UNIVERSITÀ DEGLI STUDI DI NAPOLI "FEDERICO II"

Scuola Politecnica e delle Scienze di Base

Area Didattica di Scienze Matematiche Fisiche e Naturali

Dipartimento di Fisica "Ettore Pancini"

Laurea Magistrale in Fisica

Study, design and characterization of superconducting quantum devices based on tunnel ferromagnetic Josepshon junctions

Relatori:
Francesco Tafuri
Davide Massarotti
Roberta Satariano

Candidato:
Francesca Calloni
Matr. $N94000677$

Anno Accademico 2023/2024

Contents

Introduction

Over the past two decades, quantum technologies have made significant progress in strategical areas such as sensing, cryptography, telecommunications, and computing [1][2][3]. For what concerns quantum computation, superconducting qubits are one of the leading platforms to build a quantum computer capable of performing computation tasks beyond modern supercomputers. Prototype algorithms, including Google's pioneering experiment, have been demonstrated on superconducting qubits in the noisy intermediate-scale quantum (NISQ) technology era [4]. However, despite these exciting achievements, going beyond the current size of today's quantum processor consisting of few hundreds qubits to a scalable quantum processor with thousands of qubits is far from a trivial challenge. For istance, although the transmon [5] is the most widely adopted superconducting qubit design, it still suffers from architectural issues that need to be addressed. Transmon qubit frequency can be tuned using magnetic flux threading a loop geometry in a d.c. SQUID (Superconducting Quantum Interference Device), that allows faster gate operations, but introduces a sensitivity to random flux fluctuations (flux noise), thus leading to dephasing times of the order of tens of μs. Moreover, the milliamper currents that are used for flux tunability also cause crosstalk between qubits and heating. So far, superconducting quantum circuits have almost exclusively relied on aluminum-aluminum oxide-aluminum (Al/AlO_x/Al) tunnel Josephson junctions (JJs) [6][7]. Hybrid superconductor-semiconductor structures, such as two-dimensional electron gas (2DEG), van der Wals materials and semiconducting nanowires[8][9], have provided an alternative tuning of the qubit frequency without introducing flux-noise by exploiting a gate voltage in the so-called gatemon architecture. The gatemon qubits set an important milestone by demonstrating that hybrid Josephson devices can be integrated into qubits to gain new frequency qubit knobs. Among unconventional Josephson devices, in the last decades the physics of magnetic Josephson Junctions have been widely investigated. However, the use of such junctions has been limited to phase shifters and spintronic applications [10][11][12], placing little emphasis on their role in quantum computing due to their inherent high quasiparticle dissipation, which can affect the qubit performance. Recent advances in coupling ferromagnetic layers with insulating barriers inside the JJ (Superconductor-Insulator-superconductor-Ferromagnet-superconductor: SIsFS) and leveraging intrinsic insulating ferromagnetic materials have led to magnetic JJs with high quality factors and low quasiparticle dissipation [13][14]. Therefore, in our group we have proposed to integrate a tunnel magnetic Josephson Junction into a trasmon circuit to allow a tuning of the qubit frequency by means of magnetic field pulses, in the so-called ferrotrasmon architecture [7]. Most importantly, in principle a single magnetic Josephson junction can replace the SQUID set-up, thereby improving the scalability of the entire quantum circuit. Finally, this research activity goes beyond a mere search for the best qubit candidate; it also promotes an advancement toward a better understanding and control of the phenomena occuring at S/F interface in magnetic Josephson Junctions, such as the inverse proximity effect [15].

In this thesis, we have focused on two fundamental steps towards the experimental validation of the ferro-transmon: the design of flux lines for an on-chip control of this hybrid qubit and the characterization of tunnel SIsFS JJs suitable for the final layout. The first chapter presents the basic principles of superconductivity and the Josephson effect and then introduces standard superconducting qubits with a special focus on the transmon design. The second chapter will present an overview of the properties and functionalities of Magnetic Josephson Junctions (MJJs), beginning with an examination of the fundamental concepts of ferromagnetism and subsequently elucidating the operational principles of SIsFS JJs. As it will be discussed in more detail at the end of the second chapter, these SIsFS JJs possess the capability to combine the memory properties of standard SFS JJs with the tunnel behaviour of SIS JJs. As mentioned above, this unique combination offers a promising alternative for the control of qubit frequency in the ferrotransmon architecture. The third chapter is devoted to the description of the experimental apparatus employed to characterize the junctions under investigation, including the dilution cryostat. The experimental results are discussed in the fourth chapter. We first discuss the transport properties of SIsFS junctions with a ferromagnetic layer of Permalloy ($Ni_{80}Fe_{20}$) and compare with standard SIS tunnel JJs. In order to optimise the magnetic properties of the junction, we then characterize SIsFS junctions with a ferromagnetic layer of $Ni_{77}Fe_{11}Gd_3Nb_9$. In contrast to standard flux-tunable transmons, which feature flux-bias lines inductively coupled to d.c. SQUID loops, SIsFS JJs require in-plane magnetic field to be switched. At the end of the chapter, we thus propose three designs of flux lines to provide an in-plane magnetic field. The simulations show the range of magnetic fields that can be actually applied for a on-chip control of the SIsFS JJs and thus provide a benchmark for optimizing the ferromagnetic barrier in the SIsFS JJs. By studying both the ferromagnetic barrier in the SIsFS JJs and the flux line layouts, we have thus carried fundamental steps toward the optimization of the overall design of the ferrotransmon and its scalability.

Chapter 1

Conventional Josephson junctions

In this chapter, the principles and notions of the Josephson Effect for conventional tunnel junctions will be introduced, in order to better understand the peculiarities of hybrid ferromagnetic Josephson junctions reported in the following Chapters. After a brief recall of the general aspects of superconductivity, the phenomenology of the Josephson effect will be introduced, focusing on the transport properties and on the electrodynamics of Josephson junctions as a function of temperature and magnetic field. Moreover, the key role of the Josephson junctions in superconducting quantum circuits will be discussed at the end of the chapter.

1.1 Recalls on Superconductivity

Superconductivity occurs when certain materials, brought below a specific critical temperature T_C, present zero resistivity and perfect diamagnetism. Its first observation dates back to 1911 to the experiment of Kamerlingh Onnes, who observed that the electrical resistance of various metals such as mercury disappears below a critical temperature textitT_C, which is characteristic of the material, as shown in Figure 1.1[16].

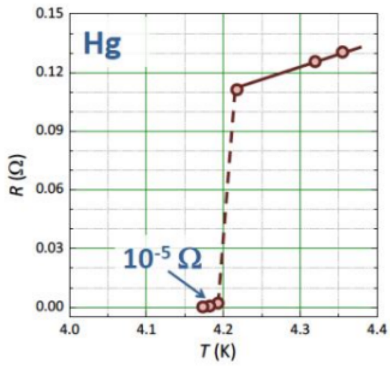

Figure 1.1: Dependence of the resistance on the temperature of a mercury sample: example of transition to zero resistance. The sample is in the superconducting state up to the critical temperature of $T_C = 4.2K$. Above T_C, the sample is in the normal state and the resistance takes a leap increasing almost linearly with temperature.[17]

The perfect diamagnetism behavoir, known as *Meissner effect*, was observed in 1933 by Oschenfeld and Meissner [18]: when a weak magnetic field $\vec{B}$ is applied, the magnetic field lines are fully expelled, i.e., the magnetic susceptibility $\chi = -1$. The ejection of the magnetic field is due to the generation of surface screening currents, which in turn induce a magnetic field that balances the external magnetic field. The *Meissner effect* is schematized in figure 1.2 and it is described by the second London equation [16][19]:

$$\nabla^2 \vec{B} = \frac{1}{\lambda_L^2} \vec{B}. \tag{1.1}$$

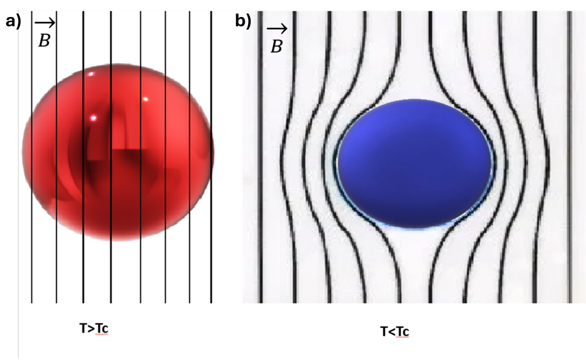

Figure 1.2: a) Above the critical temperature T_C, the superconductor is in the normal state and the magnetic field $\vec{B}$ penetrates the sample. b) For $T < T_C$, the sample enters the superconducting state and the magnetic field lines are expelled.

In the equation 1.1 λ_L is the London penetration depth that determines the length scale over which the magnetic fields are exponentially screened from the surface of the superconductor [20]:

$$\lambda_L^2 = \frac{n_s 4\pi e^{*2}}{m^* c^2}, \tag{1.2}$$

where n_s is the superfluid density and e^* and m^* are the charge and the mass of the superconducting carriers involved in the conduction mechanism, respectively. The London penetration depth depends on the material, as n_s the superfluid density of the superconductor. It is experimentally found the following temperature dependence of the London penetration depth [16]:

$$\lambda_L(T) = \lambda_L(0)\left[1 - \left(\frac{T}{T_c}\right)^4\right]^{(-1/2)}. \tag{1.3}$$

It increases slowly at low temperatures and diverges as it approaches the transition temperature T_C. It's a fundamental quantity for the sizing of superconducting materials and their applications [18].

Another characteristic property of superconductors is the quantization of the flux in a topologically non-connected superconductor: the flux of the magnetic field can assume only integer values of the quantity $\Phi_0 = h/2e$. The presence of the factor 2 suggested that the charge carriers of the supercurrent were two electrons and this later gave rise to the idea of Cooper pairs [18]. However, the decisive step in understanding the microscopic mechanism of superconductivity is due to Bardeen-Cooper-Schrieffer (BCS) theory. In the BCS theory at low temperatures, it was shown that a weak phonon-mediated attractive interaction between electrons causes the formation of bound pairs, the so-called Cooper pairs. In a conventional bulk superconductor (s-wave superconductor), they consist of two electrons with opposite spin and momentum close to Fermi momentum. The total spin of a Cooper pair is zero, which means that it represents a Bose particle (that is, obeys Bose-Einstein statistics). Therefore, the pairs of electrons can be described by a single macroscopic wave-function, thus supporting the previous phenomenological theories [16].

The Ginzburg-Landau theory (GL) provides a general approach to describe second-order phase transitions involving spontaneous symmetry breaking [16] [19]. According to this theory, a phase transition of the second order occurs when the order parameter changes discontinuously at the transition temperature T_C. By decreasing the temperature below $T < T_C$, the system performs a phase transition and passes from a highly disordered and symmetric state to an ordered one, a spontaneous symmetry breaking therefore occurs, for which the system chooses to place itself in a state of minimum energy. The GL theory introduced quantum mechanics into the description of superconductors. It assigned to the entire number of superconducting electrons a wavefunction depending on a single spatial coordinate $\psi(r)$. By expressing the free energy density in a series expansion of $|\psi|^2$ and solving a variational problem, the order parameter satisfies the Ginzburg-Landau equations [19]:

$$\alpha\Psi + \beta(\Psi)|\Psi|^2 + \frac{1}{2m}(-i\hbar\nabla - 2e\vec{A})^2\Psi = 0, \tag{1.4}$$

$$\vec{J} = \frac{e}{m}\left(\Psi^*(-i\hbar\nabla - 2e\vec{A})\Psi + .c.\right), \tag{1.5}$$

where $\vec{A}$ is the vector potential, m is the mass of the electron and e is its charge. The current density J is related to the vector potential and to the superfluid density. The parameter β is a constant, while $\alpha(T) = 1 - (T/T_c)$[16]. The Ginzburg–Landau theory also introduces another characteristic length ξ, the so-called coherence length, which indicates the average distance at which the electrons of the Cooper pair are located:

$$\xi = \sqrt{\frac{\hbar^2}{2m * |\alpha|}}, \tag{1.6}$$

where α is one of the phenomenological constants of the Ginzburg–Landau theory. From the GL equations it appears that it is the length along which variations in the $|\psi|$ are appreciated.
By considering the temperature dependence, it's possible to distinguish two regimes:

$$\xi = \frac{\hbar^2}{2m|\alpha_0|}\begin{cases} \left(\frac{T}{T_c} - 1\right)^{1/2} T > T_c \\ \left(1 - \frac{T}{T_c}\right)^{1/2} T < T_c. \end{cases} \tag{1.7}$$

By comparing the coherence length and the London penetration length with the ratio $\kappa = \lambda_L/\xi$, we can classify two different types of superconductors when an external magnetic field is applied: type-I and type-II superconductors.

- if $\kappa < \frac{1}{\sqrt{2}}$, the superconductor is type-I: it has a linear magnetization $\vec{M}$ as a function of $\vec{H}$ up to a certain critical field value H_C, beyond which the superconducting state is destroyed and the material returns to the normal state.
- if $\kappa > \frac{1}{\sqrt{2}}$ the superconductor is type-II. These superconductors exhibit diamagnetic behavior up to a certain critical field $\vec{H}_{C1}$; above $\vec{H}_{C1}$ they have a mixed superconducting/normal behavior, whereby the field lines "pierce" the superconductor and vortices are created carrying a flux quantum $\Phi_0 = \frac{h}{2e}$, known as Abrikosov vortices [20]. When $\vec{H}$ is also larger than $\vec{H}_{C2}$, there is complete penetration of the field, again resulting in the destruction of the superconducting state.

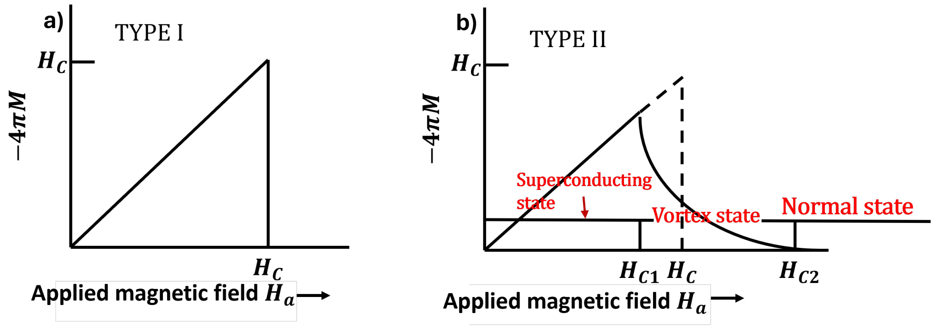

Figure 1.3: In panel a) it is reported the behavior of $\vec{M}$ as a function of $\vec{H}$ for a type-I superconductor, for $\lambda_L < \xi$; in panel b) it is reported the behavior of $\vec{M}$ as a function of $\vec{H}$ in a type-II superconductor, $\lambda_L > \xi$

1.2 The Josephson effect

The Josephson effect, predicted by Bryan Josephson in 1962 [21] and experimentally observed in 1963[22], is a macroscopic quantum phenomenon in a device known as Josephson Junction (JJ). In the simplest case, this device is made up by two superconducting electrodes, with associated wave functions $\Psi_1 = |\Psi_1|e^{i\phi_1}$ and $\Psi_2 = |\Psi_2|e^{i\phi_2}$, separated by a thin insulating barrier, with thickness of the order of 1 nm, as schematized in figure 1.4.

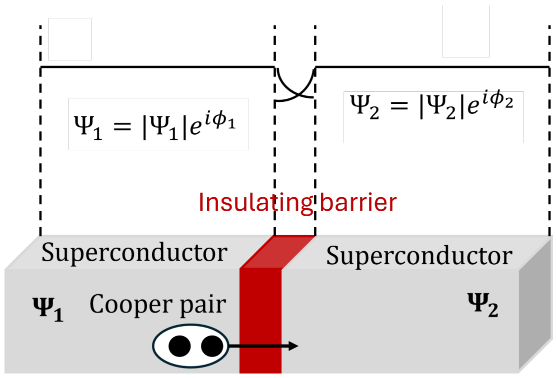

Figure 1.4: Sketch of a Josephson junction and of the macroscopic wave-functions of the two electrodes $\Psi_1 = |\Psi_1|e^{i\phi_1}$ and $\Psi_2 = |\Psi_2|e^{i\phi_2}$ and $\rho_{1/2} = |\Psi_{1/2}|^2$ is the density of Cooper pairs. The two wave-functions overlap in the barrier region.

The Josephson effect is a direct manifestation of the macroscopic quantum coherence of the superconducting state and describes the flow of a supercurrent, carried by Cooper pairs, through a nanometric barrier that separates two superconductors, without a voltage drop, as shown in Figure 1.4. The effect exists as long as the tails of the wave functions overlap. The JJs can thus differ in layout, geometry and materials of the barriers. In this thesis work, the physical principles regarding junctions with an insulating barrier (SIS) and ferromagnetic barrier (SIsFS) will be outlined. The Josephson effect is governed by two equations, which relates the supercurrente I_s and the voltage V to phase drop V across the junction $\phi = \phi_1 - \phi_2$ [18]:

$$I_S = I_C sin\phi \tag{1.8}$$

$$\frac{\partial\phi}{\partial t} = \frac{2eV}{\hbar}, \tag{1.9}$$

where $\hbar$ is the reduced Planck constant. I_C is the critical current and represents the maximum supercurrent that the junction can sustain and depends on the temperature, the magnetic field and the structure of the junction [23]. The first Josephson equation defines the current-phase relation of the device, which determines its fundamental properties. When the junction is current biased with a value below I_C, the junction is in the supercurrent branch, as shown in 1.5, the supercurrent depends only the phase difference between the two superconductors ϕ. For $I_s > I_C$, the junction transits to the resistive state and a finite voltage is observed so that the phase difference evolves with time.

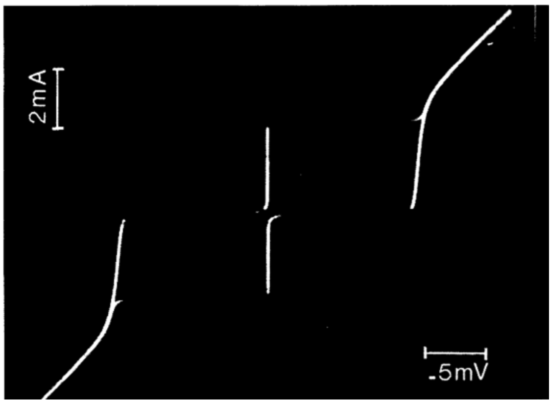

Figure 1.5: Current-voltage Characteristic of a Josephson junction: when a current bias at a junction is below the critical value, the junction is in the superconducting branch. For currents $I > I_C$, the junction transitions to a resistive state [24].

For unconventional systems, the equation 1.8 should be generalized in order to take into account also higher harmonics [25][26]:

$$I(\phi) = \sum_{n\geq 1} I_n sin(n\phi). \tag{1.10}$$

In presence of a voltage drop V_{DC} at the sides of the junction, it follows by integration of 1.9 that the phase varies linearly in time [25]:

$$\phi = \frac{2\pi}{\Phi_0}\int_0^t dt' V_{DC} = \frac{2\pi}{\Phi_0} V_{DC} t + \phi_0 = \omega_j t + \phi_0. \tag{1.11}$$

The Josephson current thus oscillates sinusoidally in time, at the Josephson frequency ν_j in the regime of microwaves ($10^9 - 10^{13}$Hz) ranging V tipically 10^{-6} to 10^{-2} :

$$I_S = I_C sin(\omega_j t + \phi_0). \tag{1.12}$$

In presence of microwave irradiation of a junction biased with a d.c. current, the interaction between the microwave signal and the a.c. Josephson current leads to the appearence of current steps at constant voltages:

$$V_n = n\frac{\Phi_0}{2\pi}\omega_j, \tag{1.13}$$

where n is an integer number. Such steps have been observed for the first time by Shapiro in 1963 and are thus called Shapiro steps [27].
A Josephson junction is able to store energy in the superconducting state, the so-called Josephson energy, that can be considered as the binding energy due to finite overlapping of the two wave functions:

$$E_J = I_c\frac{\hbar}{2e}. \tag{1.14}$$

This expression can be derived on the basis of simple thermodynamical arguments [21] or of microscopic theory [28]. In the thermodynamic approach, the free energy change due to the work done by the current generators is: $dF_1 = IV_1dt$ and $dF_2 = IV_2dt$. So, the energy associated with the barrier will be given by $dF = dF_2 - dF_1 = I(V_2 - V_1)dt$, substituting 1.8 and 1.9 and integrating:

$$F(\phi) = \frac{\hbar}{2e}I_c cos\phi + constant. \tag{1.15}$$

By imposing F= 0 for $\phi = 2n\pi$, with n an integer, it is ensured that no current flows into the junction. It can be seen that this leads to the conclusion that $F(\phi) = E_J(1 - cos\phi)$, which is consistent with the 1.14.
Moreover, the insulating layer of the JJ constitutes a capacitor with flat and parallel faces with an associated charging energy $E_C = \frac{e^2}{2C}$. Depending on the ratio E_J/E_C, we can distinguish two different regimes: phase regime and charge regime, as it will be explored in details in the following sections.
The expression for the critical current and its temperature dependence can be derived on the basis of the microscopic BCS theory in the tunnel limit, as first shown by V. Ambegaokar and A.Baratoff [29]. The resulting Ambegaokar-Baratoff (AB) relation for the critical current of the junction reads:

$$I_c(T) = \frac{\pi}{2eR_N}\Delta(T)tanh\left(\frac{\Delta(T)}{2k_BT}\right), \tag{1.16}$$

where R_N is the normal-state resistance and Δ is the superconducting gap [29]. For $T = 0$, Eq. 1.16 takes the following simplifed form:

$$I_c(0) \simeq \frac{\pi\Delta}{2eR_N}. \tag{1.17}$$

Finally, substituting into Eq. 1.8 $d\phi/dt$ with V according to Eq. 1.9: $dI_s\ dt = I_0cos\phi\frac{2\pi}{\Phi_0}V$. With dI_s/dt proportional to V , this equation describes an inductor. By defining a Josephson inductance L_J according to the conventional definition $V = L_JdI_s/dt$, one finds $L_J = \frac{\Phi_0}{2\pi I_c cos\phi}$. The $1/cos\phi$ term reveals that this inductance is nonlinear. It becomes large as $\phi \to \pi/2$, and is negative for $\pi/2 < \phi < 3\pi/2$. The inductance at zero bias is $L_{J0} = \Phi_0/2\pi I_c$. An inductance describes an energy-conserving circuit element[30].

1.2.1 Magnetic field effect

By applying a magnetic field, different phenomena are observed in a Josephson junction, all these effects are induced by the phase variation due to the external magnetic field. Geometry of the junction, nature of the electrodes or of the barrier and their possible inhomogeneities determine a distinctive spatial distribution of the critical current density across the junction barrier, and are reflected in the magnetic dependence of the I–V curves. To establish the relation between the supercurrent passing through the junction and the applied magnetic field, we consider a planar junction and a magnetic field $\vec{H}$, perpendicular to the direction of the supercurrent, as sketched in figure 1.6.

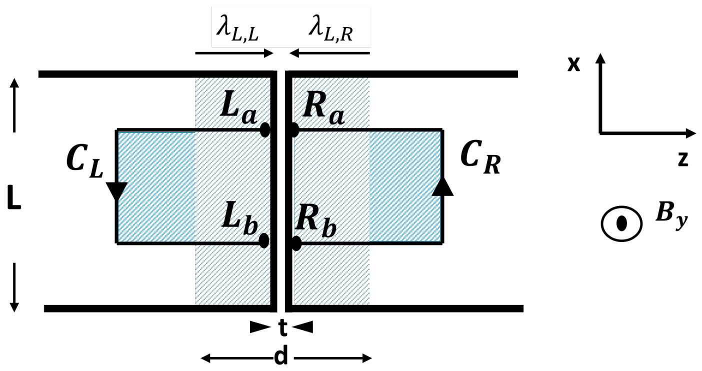

Figure 1.6: Scheme of a JJ with the contours of integration to derive the magnetic field dependence of the phase difference. The dashed areas indicate the regions where the magnetic field penetrates into the superconducting electrodes from the side where they face each other.

It is assumed that the thickness of the superconducting films is larger than λ_L and we consider the integration paths C_L and C_R to calculate the gauge invariant phase difference between two points of the barrier of coordinates x and $x+dx$. The general expression correlating the phase, the electric current and the magnetic field is:

$$\nabla\phi = \frac{2e}{\hbar}\left(\frac{m\mathbf{J}}{2e^2 n_s} + \mathbf{A}\right), \tag{1.18}$$

where n_s is the density of Cooper pairs and $\mathbf{A}$ is the vector potential; the difference in the phase drop across the junction between the positions $x, x+dx$ is given by the following expression:

$$\phi(x+\Delta x) - \phi(x) = \frac{2e}{\hbar}\oint \mathbf{A}d\mathbf{l}. \tag{1.19}$$

We note that the effects of the bulk supercurrents $\mathbf{J}$ can be neglected since $\mathbf{J}$ is perpendicular to the chosen integration path and takes on a very small value inside the superconductors. By using the Stokes' theorem, we obtain $\oint \mathbf{A}d\mathbf{l} = H_y(t + \lambda_{L,L} + \lambda_{L,R})\Delta x$ where t is the barrier thickness and $\lambda_{L,R}$, $\lambda_{L,L}$ are the London penetration depths in the two superconductors, respectively. For $\Delta x \to 0$

and assuming that the penetration length is the same for both sides λ_L, equation 1.19 leads to:

$$\frac{d\phi}{dx} = \frac{2e}{\hbar}(2\lambda_L + t)H_y. \tag{1.20}$$

The phase difference ϕ thus assumes a spatial dependence:

$$\phi(x) = \frac{2\pi H_y d_m}{\hbar} + \phi_0, \tag{1.21}$$

where $d_m = \lambda_{L,R} + \lambda_{L,L} + t$ is the magnetic thickness,i.e., the thickness penetrated by the external magnetic field B_y, and ϕ_0 is the phase difference for $x = 0$. So the spatial dependence of the critical current density is:

$$J_s = J_C sin\left(\frac{2\pi H_y dx}{\hbar} + \phi_0\right). \tag{1.22}$$

By integrating the equation 1.22 over the junction area, we obtain the analytical expression of critical current $I_c(H)$. It can be shown that a rectangular junction with a lateral size L and a uniform zero-field tunneling current distribution exhibits a dependence of the maximum supercurrent on the applied magnetic field in the form of a Fraunhofer-like diffration pattern [18]:

$$I_s(\Phi) = J_S WL\left|\frac{sin\left(\pi\frac{\Phi}{\Phi_0}\right)}{\left(\pi\frac{\Phi}{\Phi_0}\right)}\right|, \tag{1.23}$$

where the product WL is the junction area [18]. Thus, for a rectangular JJ the minima in the pattern occur at multiples integer of Φ_0, as shown in Fig. 1.7. For circular JJs with a uniform zero-field tunneling current distribution, the analytical expression of the $I_C(H)$ follows an Airy pattern:

$$I_1(K) = I_1\left|\frac{J_1(kR)}{\frac{1}{2}(kR)}\right| \tag{1.24}$$

where $I_1 = \pi R^2 J_1$, $J_1(x)$ is the Bessel function of the first kind, $k = \frac{2\pi d_m}{\Phi_0}$ and R the radius of the junction [18][23].

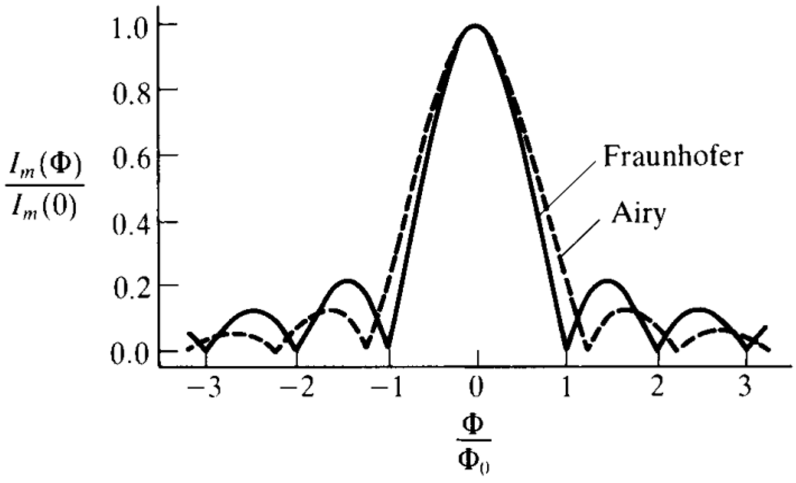

Figure 1.7: Dependence of the critical current on the external flux. The solid line follows the Fraunhofer pattern for rectangular junctions, while the dotted line is the Airy pattern for circular junctions [16].

$I_C(H)$ measurements are an important tool for characterising the quality of the junction. Deviations from the expected behaviour of $I_C(H)$, such as minima with non-zero current, suppression of the amplitude of some lobes and asymmetries of the pattern can be related to non-uniform current distribution, arbitrary orientation of the applied in-plane magnetic fields or structural fluctuations and inhomogeneities in the tunnel barrier [18].

1.2.2 Phase dynamics

Through the study of the I-V characteristics, we have a first analysis of the transport properties of the junction and of its electrodynamics. A basic tool to describe the I-V phenomenology of a large variety of weak links is the Resistively and Capacitively Shunted Junction (RCSJ) model, first introduced by McCumber and Stewart[31][32]. A Josephson junction can be schematized into an equivalent circuit having in parallel a capacitor (C), a resistor (R), and a nonlinear element with a sinusoidal current-phase relation, as shown in the figure 1.8 [23].

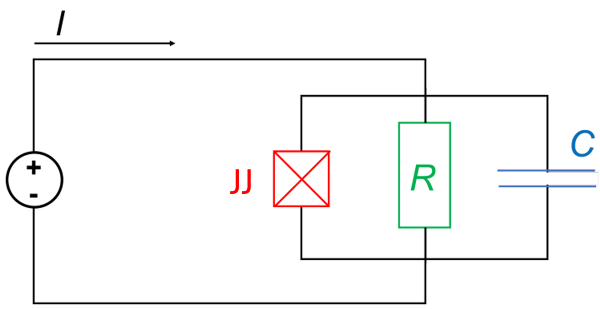

Figure 1.8: The equivalent circuit of a current biased Josephson junction according to the RCSJ model: the parallel of a JJ, a capacitance C and a resistance R.

If the junction is current-biased, the circuit equation, neglecting the noise term, is:

$$I = I_C sin\phi + \frac{V}{R} + C\frac{dV}{dt} = \tag{1.25}$$

$$I_C sin\phi + \frac{1}{R}\frac{\hbar}{2e}\frac{d\phi}{dt} + C\frac{\hbar}{2e}\frac{d^2\phi}{dt^2}. \tag{1.26}$$

By replacing the Josephson relation in equation 1.26, we can rewrite the equation that describes the phase dynamics:

$$C\left(\frac{\hbar}{2e}\right)^2\frac{d\phi^2}{dt^2} + \frac{1}{R_N}\left(\frac{\hbar}{2e}\right)^2\frac{d\phi}{dt} + \frac{dU(\phi, I)}{dt} = 0, \tag{1.27}$$

where $U\left(\phi, I\right)$ is the washboard potential represented in figure 1.9 given by the relation:

$$U(\phi, I) = -E_J\left(cos\phi + \frac{I}{I_C}\phi\right), \tag{1.28}$$

with E_J the aforementioned Josephon energy. The washboard potential depends on the bias current I: for $I = 0$, the potential is cosinusoidal; for $I > 0$, the profile acquires a certain tilt determined by the value of ratio I/I_c.

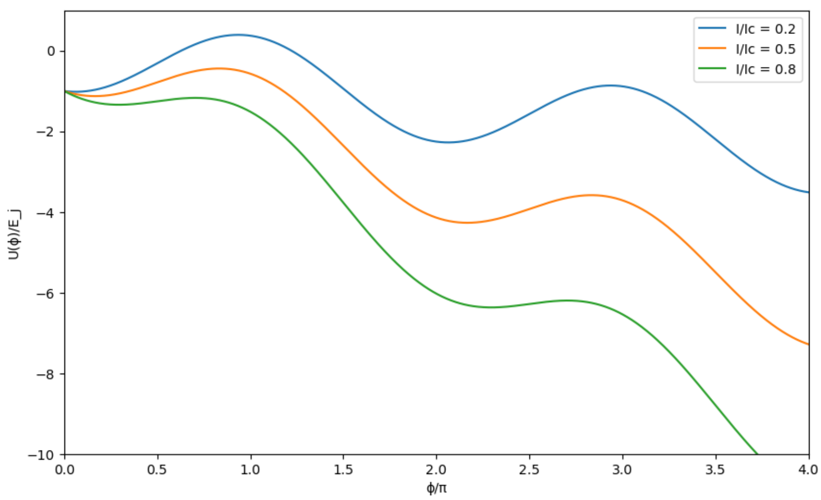

Figure 1.9: The trend of potential $U(\phi)/E_J$ for different values of the constant $\alpha = I/I_c$.

The dynamics of the Josephson phase can be studied in analogy with the motion of a particle of mass $M = C(h/2e)^2$ subject to a damping $\eta = 1/R_N(h/2e)^2$ and moving in a tilted washboard potential $U(\phi, I)$:

- if the JJ is biased with a current $I < I_C$, the Josephson phase is trapped in one of the cosine minima, around which it oscillates locally with the plasma frequency $\omega_p = \sqrt{\frac{2eI_C}{\hbar C}}$. Since the average value of the phase in time is constant, there is no voltage drop and the junction is thus in the superconducting phase that corresponds to the supercurrent branch of the I-V.

- increasing the bias current, $I \geq I_C$, the tilt of the potential is such as to transform the minima into inflections; the phase particle rolls down along the tilted potential and the phase thus, changes over time leading to a voltage V across the JJ. The transition to the resistive state occurs at a finite voltage V_{sw} which, in the ideal case, is the sum of the gaps of the two electrodes $V_g = |(\Delta_1 + \Delta_2)/e|$.

- reducing the bias current, $(I < I_C)$, the phase remains in a non-ohmic resistive state. This state corresponds to the subgap branch of the I-V curve. The junction continues to stay in this state until the current reaches a specific value known as the retrapping current, denoted as I_r.

To take into account the dissipative effects of a JJ, the Stewart-McCumber parameter is introduced [31][32]:

$$\beta_C = \frac{\omega_c^2}{\omega_p^2} = \frac{2eI_C}{\hbar} C R_N^2 \tag{1.29}$$

linked to the quality factor Q of the circuit: $Q = \frac{\omega_c}{\omega_p} = \sqrt{\beta_C}$. $\omega_C = 1/\tau_C ==$ $(2e/\hbar)V_c$ is the frequency linked to the characteristic time τ_C of the circuit. Depending on the value of β_C, the following regimes are distinguished:

- Overdamped junctions for $\beta_C << 1$. These are JJs with a small capacitance, very dissipative and therefore not suitable for quantum devices, as it will better clarified in the next chapter. An overdamped junction has a small capacitance hence a small moment of inertia and is thus immediately re-trapped in a minimum of the washboard ($I_r \sim I_C$), as shown in Figure 1.10 a. Overdamped behavior is characterized by the absence of hysteresis.

- Underdamped junctions for $\beta_C >> 1$. These are JJs with a large capacitance, so the dissipation is low and the moment of inertia is large. The particle rolls down the potential until the washboard tilt is reduced $I \to 0$. Figure 10.b shows an IV characteristic of JJ underdamped: the vertical branch in red represents the passage of the supercurrent through the junction, with a maximum value of I_C (or $-I_C$). When the current flowing through the junction exceeds the critical current value, a finite voltage value is observed at the ends of the junction and the so-called quasi-particle branch (green line in Figure 10.b) is observed, the junction returns in the zero-voltage state and the I(V) curve is hysteretic; the normal state branch is shown in blue.

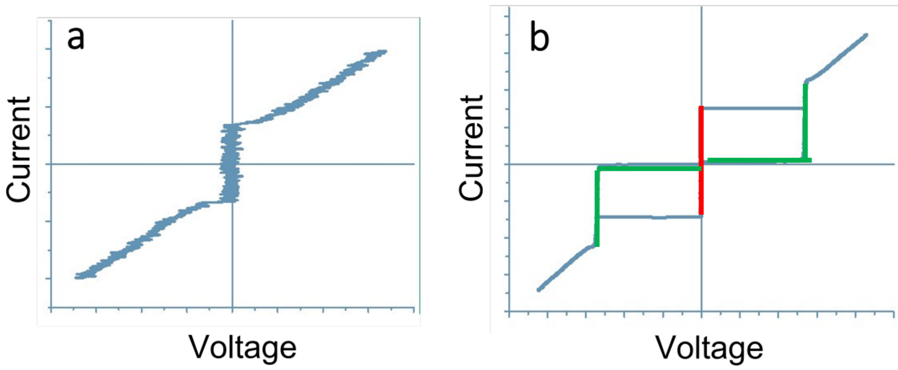

Figure 1.10: Current-voltage characteristics of (a) an overdamped and (b) underdamped JJ.

The RCSJ model is more precise in describing overdamped junctions: the capacitance C is small and equation 1.26 can be solved analitycally[23]. The voltage dependence of the subgap branch in tunnel junctions, characterized by strong non-linearity, has hindered direct comparison between experimental and theoretical curves. Consequently, alternative models have been studied such as the non linear-Resistive (RSJN) model and the Tunnel-Junction-Microscopic (TJM) model [33][34]. Both of them aim at accounting for subgap leakage currents by incorporating more sophisticated dissipative effects. For the RSJN model, the term $I_N = V/R_N$ can be approximated in two ways: considering two linear resistances depending on the voltage [25][35],

$$I_N(V) = V \begin{cases} 1/R_L, & \text{for } |V| < V_g \\ 1/R_N, & \text{for} |V| > V_g \end{cases} \tag{1.30}$$

or a dependence I on V that follows a power law:

$$I_N(V) = \frac{V}{R_N} \frac{(V/V_g)^n}{1 + (V/V_g)^n} \tag{1.31}$$

with $n >> 1$. Meanwhile, the TJM model replaces the simple sinusoidal current-phase relation and external parallel resistance with a more general expression derived from microscopic theory[25][35]:

$$I = \frac{\Phi_0}{2\pi} C \frac{\partial^2 \phi}{\partial t^2} + I_{qp} V(t) + I_{J2} V(t) cos\phi(t) + I_{J1} V(t) sin\phi(t). \tag{1.32}$$

The quantities I_{qp},I_{J1} and I_{J2} have explicit dependencies on voltage bias and temperature. Specifically: $I_{J1} sin\phi(t)$ and $I_{J2} cos\phi(t)$ correspond to processes involving phase-coherent tunneling of Cooper pairs, while I_{qp} represents the quasiparticle current [18][23].

In the discussion presented so far, the effects of fluctuations have been neglected. However, at a finite temperature, the phase particle can escape from the potential potential wells for a value of the current $I < I_C$. The escape processes can occur either by thermal activation (TA), Macroscopic Quantum Tunneling (MQT)[36][37] and phase diffusion (PD). In the first case, thermal fluctuations excite the phase particle above the energy barrier, causing the switch to the resistive state. In case of quantum tunneling, at low temperature and for junctions in the underdamped regime, the phase particle tunnels through the barrier and goes into the resistive state. In overdamped and moderately damped junctions, the phase particle can be retrapped in one of the following minima after an escape event (phase diffusion). At low bias, escape and retrapping processes can occur multiple times, leading to extensive phase diffusion [38][39]. When the tilt of the potential increases due to a change in bias current, the particle's velocity rises, allowing the junction to switch to the running state. Analyzing phase diffusion has broader implications, including understanding the motion of a Brownian particle in a periodic potential. These escape processes therefore lead to a switch to a resistive state as a function of the bias current, manifest a stochastic process and they can be fully characterized by switching current distributions (SCDs) measurements [23] [40]. Briefly these three processes can be distinguished based on the thermal behaviour of width of the distribution σ: for MQT the σ is constant, TA is increasing, PD is decreasing [41]. At first glance, it might be assumed that with increasing temperature, fluctuations in switching current would widen the distribution. However, in the PD regime, distributions become more symmetric. This occurs because there's a current range where escape and retrapping processes overlap, resulting in the truncation of the tail of the switching current distribution (SCD) [37][42].

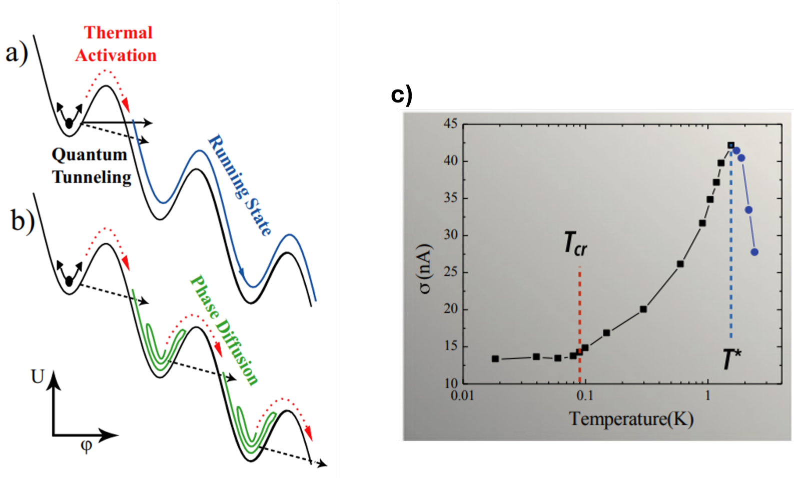

Figure 1.11: Escape process : **a)** the phase particle overcomes the barrier in the washboard potential by Thermal Activation (TA) or by Macroscopic Quantum Tunneling (MQT) and then rolls in the running state; **b)**: retrapping processes may occur for intermediate levels of dissipation, resulting in a phase diffusion (PD) regime [23]. **c)** The temperature dependence of the standard deviation, σ, of the switching current distributions. Three distinct regimes can be identified, namely: (I) MQT for $T < Tcr$, with σ constant, (II) for $T_{cr} < T < T^*$ TA with σ increasing and (III) PD for $T > T^*$, σ decreases [40].

1.3 Josephson junctions for quantum device: the transmon qubit

In the previous paragraphs the basic concepts of the Josephson effect and the physics of Josephson junctions have been presented; through a Josephson junction we can manipulate and measure the macroscopic quantum phase difference between two superconducting electrodes. This unique feature can be used to transfer on a circuit the quantum mechanics laws commonly applied to microscopic entities [43]. In particular, the study and use of JJs is being widely investigated in superconducting qubits: in fact their fabrication appears to be more advantageous compared to qubits based on atoms or ions and their manipulation is simpler [44]. In fact superconducting qubits, acting as artificial atoms, have configurable energy-level spectra determined by circuit element parameters. This parameter space allows predictable performance in terms of transition frequencies, anharmonicity, and complexity [6].
The theory for the quantized Josephson junction is defined by assuming that ϕ and the number of Cooper pairs n are operators that satisfy the commutation relation[6]:

$$[\hat{\phi}, \hat{n}] = i. \tag{1.33}$$

The mechanical analogue of the tilted washboard potential thus turns into an analogue of a quantum-mechanical description of a particle in a periodic potential, following the correspondence described in table 1.1[45] :

Particle	Josephson junction
$H = \frac{p^2}{2m} - Ucos(\frac{x}{a}) - Fx$	$H = \frac{(Q-Q_g)^2}{2C} - E_J cos(\phi) - \frac{\hbar}{2e} I_b \phi$
Cordinate x	phase ϕ
momentum p=$-\frac{\hbar}{i}\partial_x$	$\propto$ charge $\frac{\hbar Q}{2e} = -2ei\partial_\phi$
velocity v=$\frac{dx}{dt} = \frac{p}{m}$	$\propto$ voltage $\frac{2eV}{\hbar} = \frac{\partial\phi}{\partial t} = (\frac{2e}{\hbar})^2 \frac{1}{C}\frac{\hbar Q}{2e}$
massa m	$\propto$ capacitance $(\frac{2e}{\hbar})^2 C$
force F	$\propto$ bias current $\frac{\hbar}{2e} I_b$

Table 1.1: Analogy between the quantities of the quantum theory of a particle in a periodic potential and the quantum theory of a Josephson junction [45].

Therefore in absence of dissipation, the behavior of a JJ can be described by an Hamilatonian H, which is a function of the phase difference ϕ and of the charge Q transferred between the electrodes:

$$H = \frac{(Q - Q_g)^2}{2C} - E_J cos(\phi) - \frac{\hbar}{2e} I_b \phi, \tag{1.34}$$

where I_b is the bias current and Q_g is the gate charge [45]. As already introduced, the state of the junction is characterized by a macroscopic wave function Ψ. In the time-independent case it satisfies the Schrödinger equation:

$$4E_C(-i\partial\phi - Q_g/e)^2\Psi_n - E_J cos(\phi)\Psi_n = E_n\Psi_n. \tag{1.35}$$

This is called the Mathieu differential equation, its eigenfunctions Ψ_n are Mathieu functions and E_J is the Josephson energy [45]. Depending on the ratio E_J/E_C, we can distinguish two different regimes: phase regime and charge regime.

- for $E_J >> E_C$, the JJ operates in phase regime or 'tight-binding limit'[45]. In this regime ϕ is well defined and and Q has large quantum fluctuations;
- for $E_J << E_C$, the JJ operates in charge regime or 'nearly free-electron limit'[45]. It occurs when there are few Cooper pairs: n is well defined, and ϕ has large quantum fluctuations; therefore, the charging nature of the capacitor is dominating. In this situation the junction is known as a Cooper-pair box (CPB).

As we will show in the following, the Josephson junction is the element that provides the nonlinearity needed to turn a superconducting circuit into a qubit. There are different approaches for incorporating a Josephson junction into circuits to create a qubit.

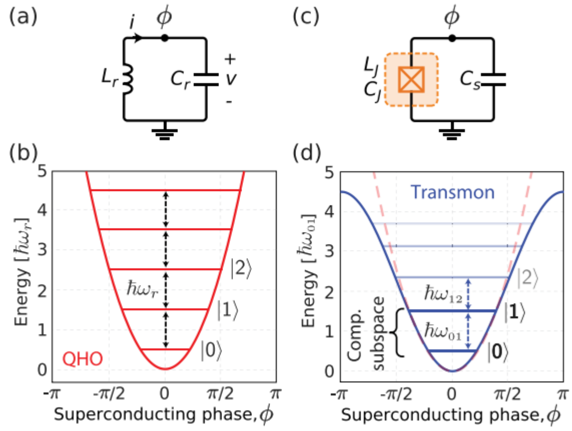

Figure 1.12: **a)** Circuit for a parallel LC-oscillator (quantum harmonic oscillator QHO), with inductance L in parallel with capacitance, C. The superconducting phase on the island is denoted as ϕ, referencing the ground as zero. **b)** Energy potential for the QHO, the energy levels, in red, are equally spaced. Therefore $\omega_{j,j+1} = \omega_{01}$ where ω_{jk} is the transition frequency between levels j and k. **c)** Josephson qubit circuit, where the nonlinear inductance L_J (represented by the Josephson subcircuit in the dashed orange box) is shunted by a capacitance, C_s. **d)** The Josephson junction introduces a cosinusoidal potential, which consequently defines non-equally spaced levels and thus categorises the system as an anharmonic oscillator, $\omega_{01} \neq \omega_{12}$[23][6].

By considering $E_L = \phi_0^2/L$, the inductive energy due to an inductance L shunting the junction, there are three relevant energies which identify the operation of a qubit and we can distinguish three basic designs for superconducting qubits: charge qubit, flux qubit and phase qubit. The circuit engineering and subsequent qubit type differentiation occurs by modification of the energy scales identified by the ratios $E_L/(E_J - E_L)$ and E_J/E_C. In the table 1.2 some configurations are reported [46]:

		$E_L/(E_J - E_L)$			
		0	$<< 1$	~ 1	$>> 1$
E_J/E_C	$<< 1$	Cooper-pair box			
	~ 1	quantronium	fluxonium		
	$>> 1$	transmon			flux qubit
	$>> 1$			phase qubit	

Table 1.2: The table shows the different configurations corresponding to the chosen ratios. The ratio E_J/E_C indicates how much the non-linearity of the system affects the charge energy; the ratio $E_L/(E_J - E_L)$ indicates how important the inductive part of the circuit is compared to the nonlinear superconducting part.

When the ratio $E_J \leq E_C$ holds, the qubit becomes highly sensitive to charge noise, which is more challenging to mitigate than flux noise. Achieving high coherence under these conditions is very difficult. Moreover, current technologies offer greater flexibility in engineering the inductive (or potential) part of the Hamiltonian. Consequently, working within the $E_J \leq E_C$ limit enhances the system's sensitivity to changes in the potential Hamiltonian [47]. This discussion will focus on the state-of-the-art superconducting qubits that fall into the regime where $E_J >> E_C$. One common approach is to shunt the junction with a large capacitor ($C_B >> C_J$), effectively reducing the qubit's sensitivity to charge noise. This circuit is commonly known as the transmon qubit ("transmission-line shunted plasma oscillation qubit") that is a modification of the CPB [48]. The circuit diagram of this qubit is shown in the figure 1.13.

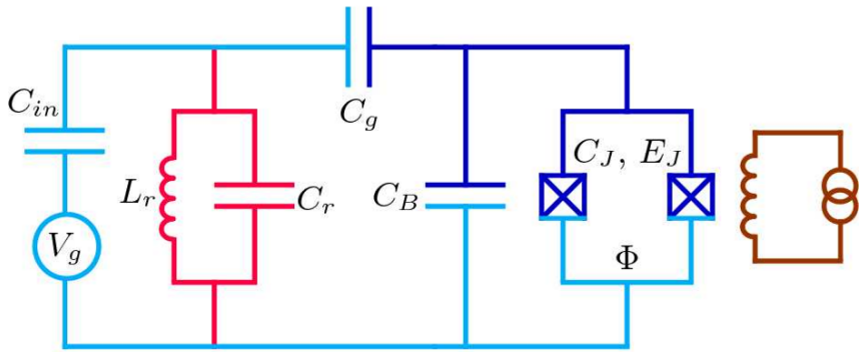

Figure 1.13: Circuit diagram of a transmon qubit[5].

The boxes indicate the two Josephson junctions of capacity C_J and energy E_J. C_B is the capacitance that is added to increase the E_J/E_C ratio and C_g is a C_g coupling capacitance for the LC resonant circuit, which is used to read the qubit state [48]; the entire system is coupled to the external electronics V_g through a capacitance C_{in}. All the capacitances of the circuit are involved in the total charging energy of the system. Adding extra capacitance over CPB reduces the charging energy E_C, bringing the ratio E_J/E_C from $\sim 10^{-1}$ to $E_J/E_C \sim 10^2$ [23]. Introducing the effective offset charge $n_g = Q_r/2e + C_gV_g/2e$, where V_g and C_g denote the gate voltage and capacitance and Q_r represents the environment-induced offset charge, the effective Hamiltonian can be reduced to a form identical to that of the CPB system [5]:

$$H = 4E_C(\tilde{n} - n_g)^2 - E_J cos(\tilde{\phi}). \tag{1.36}$$

$\tilde{n}$ and $\tilde{\phi}$ represent the number of Cooper pairs transferred between the islands and the gauge-invariant phase difference between the superconductors, respectively. The resulting energy levels are largely insensitive to fluctuations in n_g.

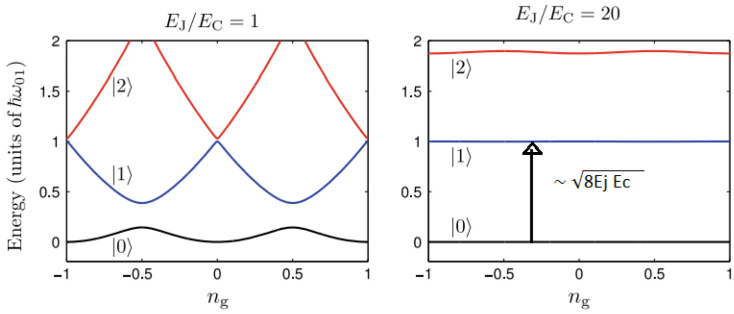

Figure 1.14: Energy levels for different values of E_J/E_C as a function of the number of Cooper pairs n_g. The level of anharmonicity depends on the ratio of E_J/E_C. Furthermore, the total charge dispersion diminishes exponentially with increasing values E_J/E_C, resulting in an attenuation of charge noise.[5].

As show in the figure 1.14, the sensitivity to charge noise decays exponentially with the root of E_J/E_C, while the anharmonicity decays with a power law: a typical ratio for the trasmon is $E_J/E_C \sim 10^2$ [49] and the main operating frequencies of transmons range from a few GHz to 10 GHz, with anharmonicities of $\approx$ 100 to 300 MHz [48]. For these E_J/E_C ratios, the low-energy eigenstates are approximately localized states in the potential well. We can gain insight by expanding the potential term $E_J(cos\phi)$ into a power series since ϕ is small [6]:

$$E_J(cos\phi) = \frac{1}{2}E_J cos\phi^2 - \frac{1}{24}E_J cos\phi^4 + O(\phi^6) \tag{1.37}$$

The leading quadratic term results in a quantum harmonic oscillator (QHO). However, the second quartic term modifies the eigensolution, disrupting the otherwise purely harmonic energy structure.
To tune the frequency of the qubit other degrees of freedom are necessary, so as to be able to perform gate operations between the qubits, putting them into resonance with each other or not [5]. Replacing the single Josephson junction in a qubit with a loop interrupted by two identical junctions, forming a DC-SQUID, a tunable Josephson energy can be achieved, which means that qubit frequency can be tuned during an experiment. The SQUID works as a single junction with an effective Josephson energy that is a function of the external magnetic flux through the SQUID loop [23]. Due to interference between the SQUID arms, the effective critical current of the parallel junctions can be adjusted by applying an external magnetic flux through the loop. This flux quantization condition ensures that the sum of branch fluxes and the applied flux equals an integer multiple of superconducting flux quanta: $\phi_1 - \phi_2 + 2\phi_e = 2\pi k$, where $\phi_e = \pi\Phi_{ext}/\Phi_0$. By controlling the external flux Φ_e, we modify the effective Josephson energy of the split transmon.

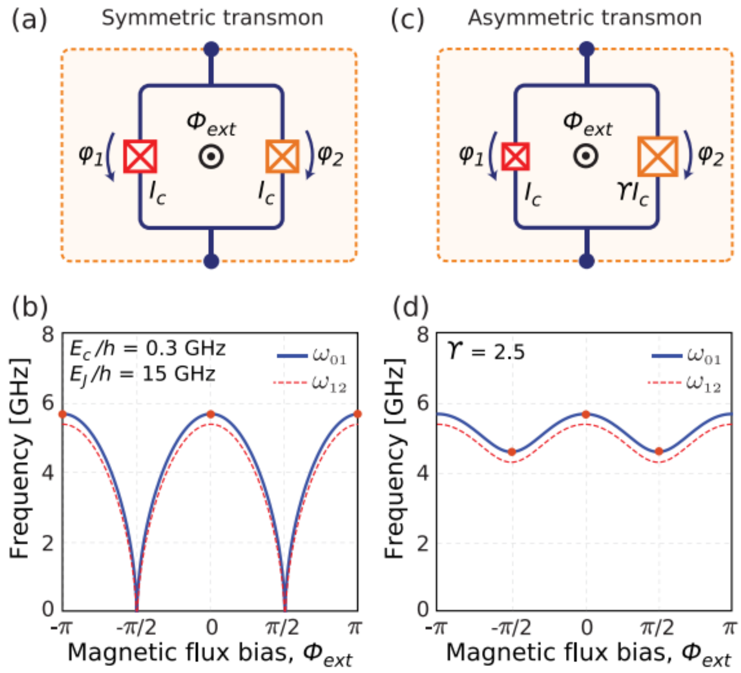

Figure 1.15: In orange box is reported the modular qubit circuit representations for capacitively shunted transmon qubit and the corresponding qubit transition frequencies for the two lowest energy states as a function of the applied magnetic flux in units of Φ_0. (a) and (b) Symmetric transmon qubit, with Josephson energy E_J shunted with a capacitor yielding a charging energy E_C (c) and (d) asymmetric transmon qubit, with junction asymmetry $\gamma = E_{J2}/E_{J1} = 2.5$ [6].

The Hamiltonian for this system includes a term related to the cosine of the external flux [6]:

$$H = 4E_C n^2 - 2E^{'}(\phi_e)_J|cos\phi|, \tag{1.38}$$

where $E^{'}(\phi_e)_J = 2E_J|cos\phi_e|$ is the effective Josephson energy that depends on $\phi_e = \pi\Phi_{ext}/\Phi_0$. Therefore, the qubit frequency can be tuned periodically with Φ_{ext}. Split transmons are sensitive to random flux fluctuations (flux noise). The slope of the qubit spectrum ($\partial\omega_q/\partial\Phi_{ext}$) indicates how strongly flux noise affects the qubit frequency. Sensitivity is nonzero except at multiples of the flux quantum ($\Phi_{ext} = k\Phi_0$, where k is an integer) as shown in Figure 1.15. Recent developments focus on reducing flux noise sensitivity while maintaining tunability [4][50]. Asymmetric split transmons achieve this by varying the junction area in the SQUID [51]. The resulting Hamiltonian introduces a small frequency-tuning range, compensating for fabrication variations without sacrificing coherence:

$$H = 4E_C n^2 - 2E_{J\sigma}\sqrt{cos^2(\phi_e) + d^2 sin^2(\phi_e)}cos\phi, \tag{1.39}$$

with $E_{J\sigma} = E_{J1} + E_{J2}$, $d = (1-\gamma)/(\gamma+1)$ is the junction asymmetry parameter and $\gamma = E_{J2}/E_{J1}$. Again, we can treat the two junctions as a single-junction transmon, with an effective Josephson energy corresponding to the second term of the equation 1.39. The tuning of the qubit frequency by means of a d.c. SQUID threaded with magnetic flux allows for the implementation of faster gate operations. However, this approach also introduces a sensitivity to random flux fluctuations, which are known as flux noise. This results in dephasing times of approximately tens of microseconds [4][50]. Furthermore, the milliamper currents that control the dc and rf lines, inductively coupled to the SQUID, allows for flux tunabilitu, but gives rise to crosstalk between qubits and heating, thus limiting integration. To date, superconducting quantum circuits have almost exclusively relied on aluminium-aluminium oxide-aluminium (Al/AlOx/Al) tunnel Josephson junctions (JJs). However, recent advances have been made in the coupling of ferromagnetic layers with insulating barriers within the JJ (superconductor-insulator-superconductor-ferromagnet-superconductor). The utilisation of intrinsic insulating ferromagnetic materials (SIsFS) has resulted in the development of magnetic JJs with high quality factors and low quasiparticle dissipation [13][14]. As will be explored in the thesis, the integration of ferromagnetic tunnel junctions enables an alternative tuning of the qubit frequency, which, in principle, can reduce the flow noise due to the presence of the squid.

Chapter 2

Magnetic Josephson junctions

This chapter will explore the properties and functionalities of Magnetic Josephson Junctions (MJJs). In the first section, we give a brief introduction on the ferromagnetism, focused on the type and appearance it takes in our devices. Then, taking into account the metallic nature of standard ferromagnetic barrier, we introduce the proximity effect as the fundamental mechanism related to transport through a S/ Normal metal (N) interface. At the end, we examine the specific features of MJJs in terms of transport properties and magnetic response to an applied field, with a special focus on Superconductor-Insulator-Superconductor-Ferromagnet-Superconductor (SIsFS) JJs. As it will be addressed at the end of the chapter, such SIsFS JJs can combine the memory properties of standard SFS JJs and the tunnel behavior of SIS JJS, thus providing an alternative control of the qubit frequency in hybrid quantum architectures, the so-called ferro-trasmon.

2.1 Ferromagnetic materials

Ferromagnetic materials are characterized by a second-order phase transition below the Curie temperature T_{Curie}. In the absence of an externally applied magnetic field, the spin system exhibits spontaneous symmetry breaking which manifests in a sharp phase transition between the ordered ferromagnetic and the disordered paramagnetic phases. For $T > T_{Curie}$, the spins do not interact with each other pointing in any direction and therefore the system is disordered and possesses complete rotational symmetry. Below T_{Curie}, the system exhibits a spontaneous alignment of all spins in a single direction, resulting in the emergence of macroscopic magnetization. In ferromagnets, the magnetization is thus the order parameter associated to the phase transition.

Near the Curie temperature, magnetization is proportional to $(T - T_{Curie})^{1/2}$ according to Landau's approach to second-order phase transition [52]. In real systems, magnetization behaves as $(T - T_{Curie})^{\beta}$, where β is not necessarily equal to 1/2 [53]. At low temperatures, the spontaneous magnetization follows the Bloch law $T^{3/2}$: the Landau approach offers a phenomenological view of second-order phase transitions, whereas the Bloch thermal behaviour can be derived from the thermal fluctuations of the magnons [54].
In this thesis, we focus on so-called band ferromagnets, which are found in alloys of 3d-transition metals, e.g., Fe, Co, and Ni, and are characterized by spin splitting of bands.

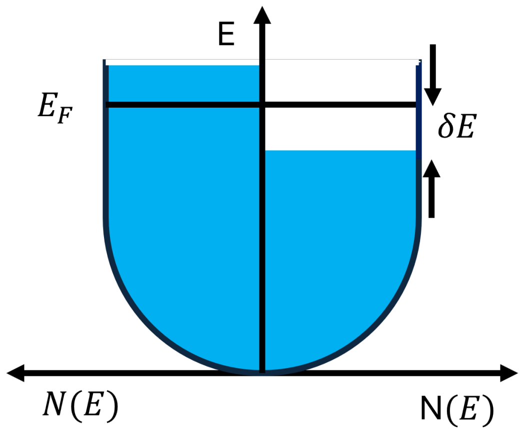

Figure 2.1: Density of states showing spontaneous splitting of energy hands without an applied magnetic field.

The majority spin-band contains more electrons, with the number density of spin-up $n^{\uparrow} = \frac{1}{2}(n + N(E_F)\partial E$; while the minority band has fewer electrons spin-down, with the number density $n^{\downarrow} = \frac{1}{2}(n - N(E_F)\partial E$ with $n = n^{\uparrow} + n^{\downarrow}$ and *N(E_F)* the density of states (DOS) at the Fermi energy E_F. Magnetization $M = \mu_B(n^{\uparrow} - n^{\downarrow})$, with Bohr magneton μ_B, depends on the difference between spin-up and spin-down densities. The resulting potential energy change Δ_{EP} accounts for exchange correlation. The system depicted in Figure 2.1, exhibits an increase in kinetic energy as a consequence of the transition of electrons from a momentum state below the Fermi momentum, $k < k_F$, to a momentum state above the Fermi momentum, $k > k_F$. Spontaneous spin-splitting occurs if potential energy is larger than the kinetic energy increase. This occurs as a result of a reduction in the number of doubly occupied degenerate states, which consequently leads to a decrease in Coulomb repulsion. The Stoner criterion thus requires strong Coulomb effects and a large density of states at the Fermi energy [55].
The alignment of the spins in the same direction is due to the exchange energy. Considering two atoms i and j having spin angular momentum $\vec{S_i}$, $\vec{S_j}$, the exchange energy is:

$$E_{ex} = -2J_{ex}\vec{S_i} \cdot \vec{S_j} cos\phi. \tag{2.1}$$

J_{ex} is the exchange integral, a constant that arises in calculating the exchange effect. It quantifies the interaction between spins. ϕ is the angle between the spins. If J_{ex} is positive, E_{ex} is a minimum when the spins are parallel ($cos\phi = 1$) and a maximum when they are antiparallel ($cos\phi = -1$). If J_{ex} is negative, the lowest energy state results from antiparallel spins. In ferromagnets, the exchange energy tends to align the spins in the same direction, as introduced above with theStoner criterion [55].

2.1.1 Domains and magnetization process

A ferromagnet at a temperature below its Curie temperature thus shows spontaneous magnetization. However, the magnetization is not necessarily homogeneous. Energetically there is a strong preference to keep the magnetization inside the material, and this typically leads to the formation of domains. In this small regions, all the magnetic dipoles are aligned parallel to each other. When a ferromagnetic material is demagnetized, the magnetization vectors in different domains exhibit varying orientations, resulting in an average total magnetization of zero. In domains, the local magnetization reaches the saturation value and each domains are separated by domain walls. Domains wall is a boundary between adjacent domains in which the magnetization vector rotates from the direction of the domain on one side to the direction of the domain on the other side. The appearence of the domain configuration is the result of minimizing the energy associated with dipolar fields: at the edges of a sample, the magnetic field diverges, creating demagnetizing fields, these fields fill space and cost energy $B^2/2\mu_0$ per cubic meter. The energy associated with the demagnetizing field is called dipolar energy:

$$E_{dip} = -\frac{\mu_0}{2} \int_V M \cdot H_d, d\tau, \tag{2.2}$$

where H_d is the demagnetizing field, when this field is outside the sample it is called *stray field*. The integral is taken over the sample volume. For an ellipsoidally shaped sample magnetized along a principal axis: $E_{dip} = \frac{\mu_0}{2} N_d M^2 V$, where N_d is the demagnetizing factor, and V is the sample volume. This dipolar energy can be saved by breaking the sample into domains, but each domain created costs energy because of the cost of the domain walls. Dipolar energy determines the type of domain wall that can form.

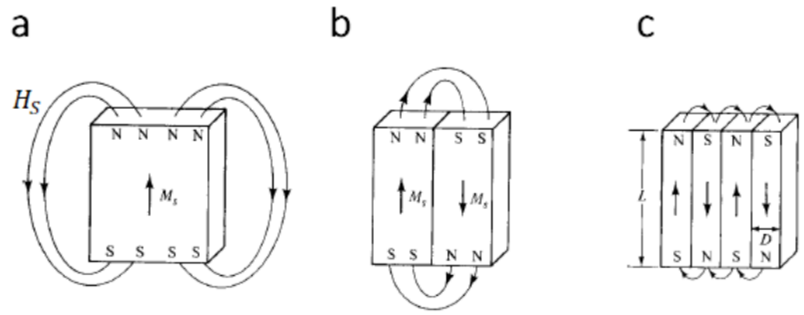

Figure 2.2: The division of a crystal into domains results from a minimization of the magnetostatic energy of the overall sample.

In the bulk, Bloch walls, in which the magnetisation rotates in a plane parallel to the plane of the wall, are favoured; conversely, Neel walls, in which the magnetisation rotates in a plane perpendicular to the plane of the wall, tend to be favoured in thin films, where there is an energy saving for keeping the magnetisation in the plane of the film. Other, more complex types of rotation do exist, but they are always a combination of the Bloch and Néel types [53].
Additionally, the magnetocrystalline anisotropy energy E_{anis} plays a role in the formation of the domain. When an external field tries to align an electron's spin, the orbit of the electron is strongly coupled to the lattice and thus resists the attempt to rotate the spin axis. E_{anis} is the energy needed to overcome this spin-orbit coupling and for a uniaxial anisotrop, E_{anis} can be described by:

$$E_{anis} = K_0 + K_1 \sin^2\theta + K_2 \sin^4\theta + \ldots. \tag{2.3}$$

Positive *K1* and *K2* values lead to an easy axis of magnetization (minimized energy at $\theta = 0$), negative *K1* and *K2* values result in an easy plane of magnetization perpendicular to the axis (minimized energy at $\theta = 90^{\cdot}$). There are preferred directions for the spin directions, so the domain walls have an energy cost, and so the final configuration of a multidomain ferromagnet is a trade-off between dipolar energy, which tends to create more domains, and the cost of crystalline anisotropy, so the formation of domains is a balance between the cost of a demagnetizing field and the cost of a domain wall.

The application of an external magnetic field H results in a modification of the magnetic configuration within the ferromagnetic material, which in turn gives rise to a change in the average magnetisation vector M. The relationship between H, and the magnetic flux density, represented by the symbol B, in a ferromagnetic material is represented by a hysteresis loop in Figure 2.3.a. During the process of magnetisation, a specimen from a multi-domain state is converted into a single-domain state along the direction of the applied field H, this process can be schematized in the Figure 2.3.b. The arrangement of magnetic vectors M_s within the domains is represented by a set of vectors originating from a common point of origin.

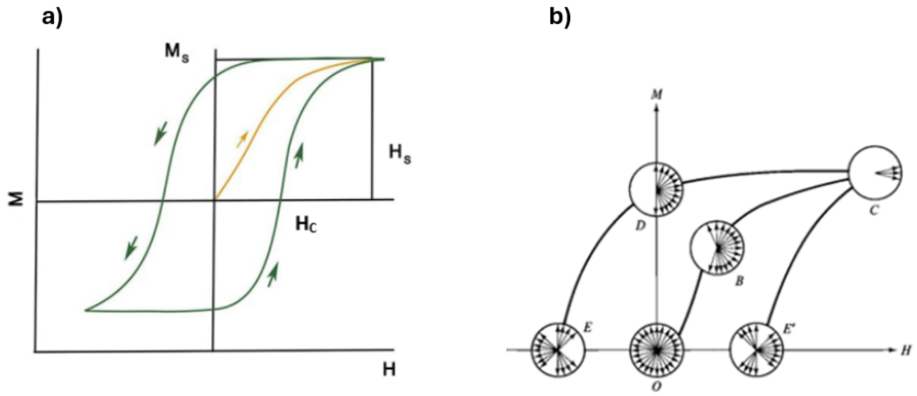

Figure 2.3: **a)**the hysteresis loop: the curvature of the hysteresis loop varies based on the type of material observed and can be narrow or wide. The graph identifies: the coercive Field (H_C), the field strength required to bring the material back to zero magnetization; the saturation Magnetization (M_S), the maximum magnetization achievable in the material; the saturation Field (H_s), the field value at which the magnetization reaches its saturation value. **b)** Distribution of domains for different magnetization states.

The point O in Figure 2.3.b represents the demagnetized State in which the domain vectors are randomly oriented. The application of a positive magnetic field results in the flipping of domains aligned in the opposite direction through the movement of the domain wall by 180 (point B). The ease of this process is contingent upon the material properties. The movement of domains can be hindered by the presence of impurities and defects. An increase in the magnetic field causes the spins within the domains to align with it, resulting in saturation (point C). When the field is removed, the domains return to their preferred orientation according to the anisotropy term, thereby generating a residual magnetisation, M_r. The application of a negative field results in the reversal of domains aligned in the positive direction, thereby producing the coercive field, H_c, at which the magnetisation becomes zero (point E). The motion of domain walls through a magnetic material depends in detail upon the metallurgical properties of the material. Domain walls can be pinned by strains in the material, by surfaces and impurities because of the magnetoelastic coupling. Domain wall pinning therefore increases coercivity. The magnetization of a ferromagnet also changes by a series of discontinuous steps due to domain boundary motion, so that very small steps are sometimes seen on the magnetization curves. This is known as the Barkhausen effect[54].

2.1.2 Proximity effect at S/N interface.

When a superconductor (S) is in contact with a normal metal (N), Cooper pairs can penetrate the normal metal, thus inducing superconducting correlations in N. This phenomenon is known as the proximity effect.

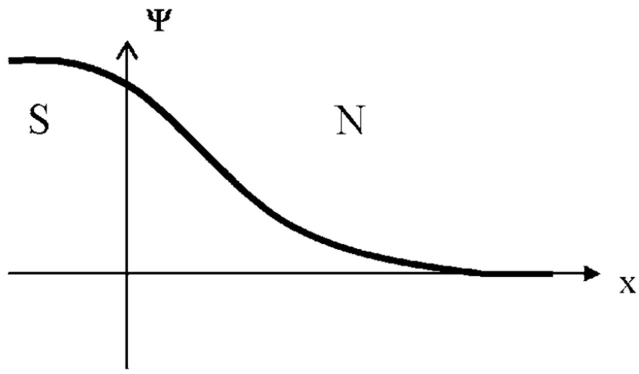

Figure 2.4: The order parameter Ψ smoothly transitions from the superconducting phase (S) to the normal state (N) without abrupt changes. In more general cases, at the interface, there can be a jump in the superconducting order parameter due to the different properties of the superconductor and the normal metal. Understanding this behavior is crucial for designing and analyzing S/N hybrid structures.

The results obtained through rigorous calculations based on the microscopic theory, are covered in detail in [19]. The GL theory offers a phenomenological account of the proximity effect, delineating the transition between the superconducting and normal phases. In the absence of a vector potential, the order parameter, which depends solely on spatial variables, reaches its maximum value (1) well inside the superconductor and vanishes well inside the normal metal. A continuous change in the order parameter is observed at the S/N interface as a function of distance x from the interface. Consequently, the initial GL equation (Equation 1.4) is simplified to the following form:

$$\xi_N(c)^2\frac{d^2\Psi}{dz^2} + \Psi = 0, \tag{2.4}$$

where ξ_N represents the coherence length in the normal metal [57]. Solving this equation with the condition $\Psi \longrightarrow 0$ well inside the normal metal, the solution is:

$$\Psi = \Psi_0 exp(-|x|/\xi_N). \tag{2.5}$$

Here, Ψ_0 represents the initial value of the order parameter in N at the S/N interface. The coherence length ξ_N characterizes how Ψ decays within the normal metal. It depends on temperature T and follows $\xi_N^2 \propto 1/(1-t)$, where $t = T/T_c$. By comparing the ξ_N with the mean free path l_N, rigorous calculations gives two different expression of the ξ_N. When the normal metal is clean, i.e., the mean free path $l_N >> \xi_N$, the coherence length is given by:

$$\xi_N(c) = \frac{\hbar v_N}{2\pi k_B T}, \tag{2.6}$$

where v_N is the Fermi velocity, and T is the temperature. In the dirty limit (l_N is smaller than ξ_N), the leakage of Cooper pairs is controlled by diffusive processes. Introducing the diffusion coefficient $D_N = \frac{1}{3} l_N v_N$, the coherence length becomes:

$$\xi_N(d) = \sqrt{\frac{\hbar D_N}{2\pi k_B T}} = \sqrt{\frac{l_N}{3}} \xi_N(c) \tag{2.7}$$

In the general case of a superconductor in contact with a true normal metal, the GL equations are not applicable to the normal region. Nevertheless, the qualitative nature of the phenomenon remains unchanged, namely, the order parameter penetrates the normal region to a certain depth, denoted by ξ_N, shown in the Figure 2.4. The proximity effect in a bilayer sandwich was treated theoretically by Kupriyanov and Lukichev [56]: they derived boundary conditions for the normal and anomalous Green's functions G(E,x) and F (E,x) at the SN interface introducing two parameters to characterize the S/N interface:

$$\begin{aligned} \gamma &= \frac{\rho_S \xi_S}{\rho_N \xi_N} \\ \gamma_B &= \frac{R_B}{\rho_N \xi_N}, \end{aligned} \tag{2.8}$$

where R_B is the resistance for unit area of the S/N interface, and $\rho_{S,N}$ are the normal state resistivity of S and N materials, respectively. The first one quantifies proximity strength, the second reflects interface transparency. As shown in Figure 2.5, γ_B determines the step in $F(x)$ at the S/N interface, while γ represents the suppression of $F(x)$ in the superconductor near the interface.

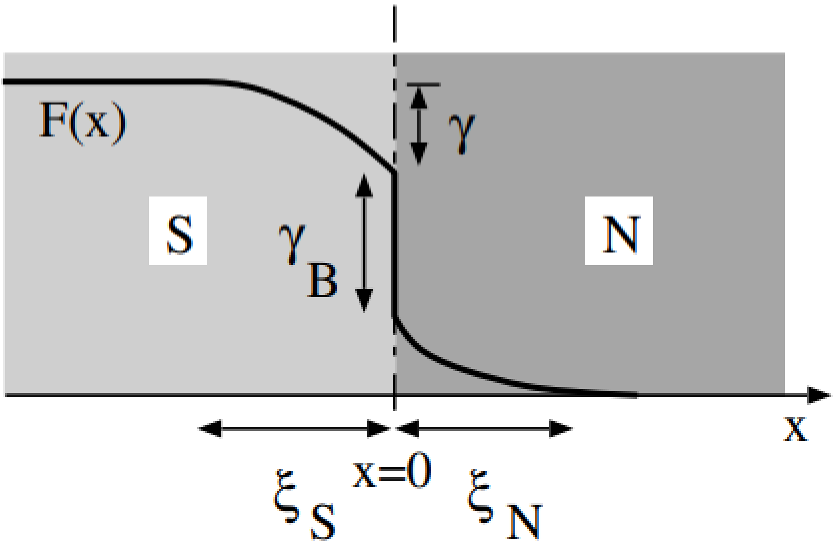

Figure 2.5: Schematic illustration of the spatial dependence of the Cooper pair density $F(x)$, Green's function, for a representative, fixed energy $E = E_0$ at an SN boundary.

At the S/N interface Andreev reflection occurs, a scattering process that explains at a microscopic level how single-electron states of the normal metal are converted into Cooper pairs, thus transforming dissipative electrical current into a supercurrent [57]. When an electron excitation in N is slightly above the Fermi level, but below the gap of the superconductor, it is reflected as a hole excitation slightly below the Fermi level. The missing charge of 2e is removed as a Cooper pair. Andreev reflection is accompanied by the injection of a Cooper pair into S: it converts electrons into holes and vice versa, altering the net charge distribution of excitations, as shown in Figure 2.6.a. In a SNS JJ, the Andreev reflection is the primary mechanism for Cooper pairs to be transferred across the N barrier. It occurs as follows: an electron approaching one of the interfaces is converted into a hole moving in the opposite direction. This process creates a Cooper pair in the superconductor. The hole is then reflected at the second interface and converted back into an electron, leading to the destruction of a Cooper pair (see Figure 2.6.b).

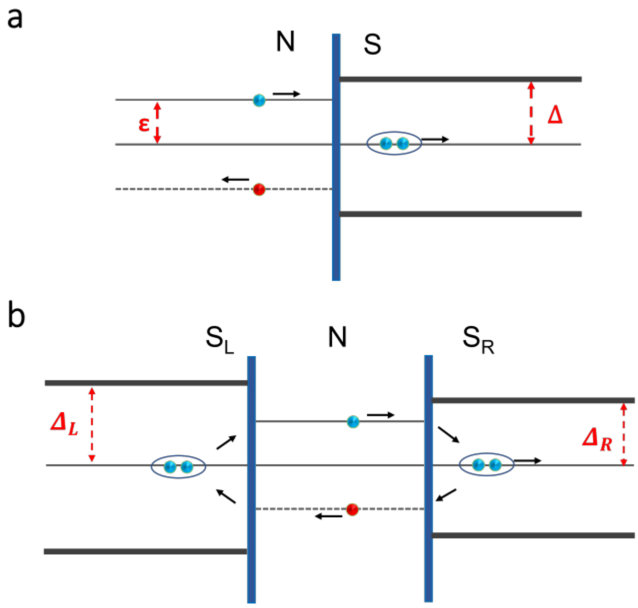

Figure 2.6: **a)** Andreev reflection at the S/N interface: an electron from the normal metal with an energy $\epsilon < \Delta$ reaches the interface and pulls an electron of energy $-\epsilon$ with opposite momentum and spin from the valence band into the superconductor, forming a Cooper pair. This second electron is taken from the valence band, leaving a hole. **b)** Andreev reflection in a SNS JJ. The electron obtains an extra phase of $\phi_L - \phi_R + \pi$ in each period.[23]

As a result of this cycle, a pair of correlated electrons is transferred from one superconductor to an other, creating a supercurrent flow across a junction [58]. Due to the electron-hole intereference in the quantum well, formed by the pairing potentials of the superconducting electrodes, standing waves with quantized energy E_{AB} appear in the weak-link region. The corresponding quantum states are referred to as Andreev bound states [58]. The spectrum of the elementary excitations of a N layer in contact with S on both sides is quantized for $E < \Delta$. The Josephson current in each channel will result from two Andreev bound states with specific phase dependent energies, lying inside the gap region $-\Delta, +\Delta$. The energy of the Andreev ground state will govern the Josephson coupling energy. The imbalance in the populations of the two Andreev bound levels finally determines the contribution to the net supercurrent flowing in each channel.[23].

The temperature dependence of the I-V curves is a crucial factor in understanding the nature of a junction. Accurate predictions allow us to assess deviations in the I_cR_n vs. T dependence from the tunnel limit represented by the Ambegaokar-Baratoff (AB) regime, which is valid for the SIS configuration. The temperature trend also depends on the ratio between the mean free path l and ξ_N for which two limits are distinguished based on the theory of Kulik and Omelianchuk [59] [60]: the dirty limit, Kulik Omelianchuk 1 (*KO1*) for $l << L_{eff} < \xi_s$, where L_{eff} is the effective length, and clean limit, Kulik Omelianchuk 2 (*K02*) for $L_{eff} << l, \xi_s$. These limits apply to point-contact Josephson Junctions and SNS junctions. In point contacts, both in the dirty and clean limits, the values of I_C at $T = 0K$ exceed the AB value, as shown in Figure 2.7. Despite this difference, the temperature dependence exhibits a downward concavity. In SNS JJs, varying the thickness of the barrier length with respect to ξ_N allows to pass from the short ($L << \xi_N$) to the long regime ($L >> \xi_N$). At the lowest temperatures, I_C saturates, while at high temperatures (near T_c), I_C exhibits a characteristic exponential dependence for large values of the ratio L/ξ_N. These two regions are connected by a curve with upward concavity at intermediate temperatures. The tail in the exponential growth and the width of the intermediate region primarily depend on L/ξ_N [61].

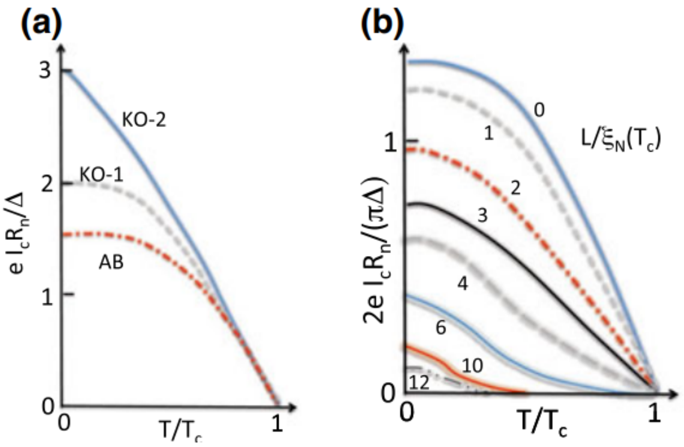

Figure 2.7: **a)** The critical current-normal resistance product as function of the temperature T, $I_CR_n(T)$ is shown for the *AB* (dashed red line), *KO1* (grey dashed line), and *KO2* (blue continuous line) limits. **b)** I_CR_n is reported in units normalized to the gap value Δ as a function of temperature (T), considering various values of the ratio between the barrier length (L) and the coherence length ξ_n [61].

2.1.3 Proximity effect at S/F interface

When superconducting correlations are induced into a ferromagnet, they exhibit distinct characteristics compared to S/N proximity systems. The proximity effect involves the penetration of Cooper pair amplitudes into a non-superconducting material. Electrons and holes with opposite spins and momenta become correlated through Andreev reflection, extending superconductivity into the non-superconducting region. In an S/N bilayer, these correlations decay exponentially with distance from the interface to the normal metal (N) due to dephasing between electron and hole wave functions as explained in the previous paragraph 2.1.2. When the interface with a superconductor consists of a ferromagnet, the up-spin electron, defined the spin orientation along the exchange field, decreases its energy by the exchange energy E_{ex}, while the down$-$spin electron energy increases by the same value. To compensate this energy variation, the up-spin electron increases its kinetic energy, while the down-spin electron decreases its kinetic energy. As a result the Cooper pair acquires a center-of-mass momentum $2\delta k_F = 2E_{ex}/v_F$ [57]. The direction of the modulation wave vector must be perpendicular to the interface, because only this orientation provides for a uniform order parameter in the superconductor. The induced superconductivity is weak and to describe it we use the linearized equation for the order parameter derived from the generalized Ginzburg-Landau functional. The solutions in ferromagnet are given by $\Psi = \Psi_0 exp(kx)$ with a complex wave vector $k = k_1 + ik_2$ [57]:

$$\begin{aligned} k_1^2 &= \frac{|\gamma|}{2\eta}\left(\sqrt{1+\frac{TT_{ci}}{T_{ci}-Tcu}}-1\right), \\ k_2^2 &= \frac{|\gamma|}{2\eta}\left(1+\sqrt{1+\frac{T_{ci}}{T_{ci}-Tcu}}\right) \end{aligned} \tag{2.9}$$

where T_{cu} is the transition temperature of the system into the uniform superconducting state and T_{ci} is the transition temperature of the system into the non-uniform superconducting state. If we choose the gauge with the real order parameter in the superconductor, then the solution for the decaying order parameter in the ferromagnet is also real:

$$\Psi(x) = \Psi_i exp(-k_1 x) cos(k_2 x), \tag{2.10}$$

with the condition $k_1 > 0$ [57].

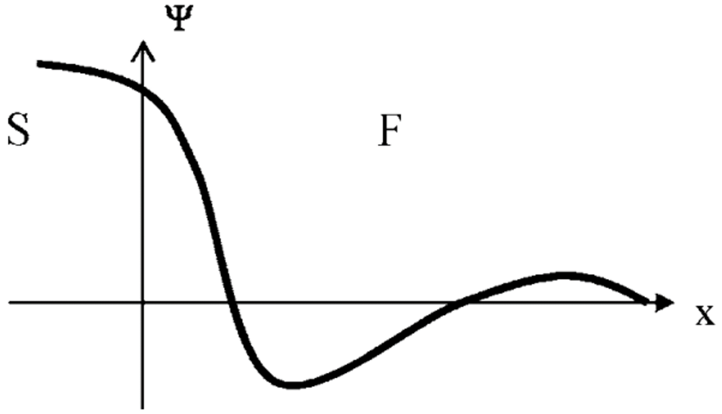

Figure 2.8: Proximity effect at S/F interface. The exchange field causes an oscillation of the order parameter

The system is thus characterized by the oscillation of the order parameter. In real ferromagnets, the exchange energy, E_{ex} is much larger than the energy scales for the superconductivity. Consequently, the gradients of the superconducting order parameter variations become significant, necessitating a microscopic approach. The Bogoliubov–de Gennes equations or Green's functions, such as the quasiclassical Eilenberger or Usadel equations, are commonly used for this purpose. In the clean limit, it can be shown that the coherence length ξ_F is given by [57]:

$$\xi_F(c) = \frac{\hbar v_F}{2(\pi k_B T + iEex)}. \tag{2.11}$$

In the dirty limit, the coherence length becomes:

$$\xi_F(d) = \sqrt{\frac{\hbar D_F}{2(\pi k_B T + iEex)}} = \frac{\sqrt{3} l_F}{\xi_F(c)}. \tag{2.12}$$

Here, D_F represents the diffusion coefficient of the ferromagnet, and l_F is the mean-free path of the F layer. In the dirty case, $\xi_{F1}(d)$ and $\xi_{F2}(d)$ are approximately 1 - 10 nm [57]. In contrast, in the clean case, ξ_{F1} is long as ξ_N (the coherence length in the normal state), while ξ_F is short, determined by the exchange energy E_{ex} [62][63].
In ferromagnetic junctions the damped oscillatory behavior of the order parameter is responsible for many interesting effects, such as $0-\pi$ transitions depending on the F layer thickness. A π junction is a Josephson junction in which the phase difference of the electrodes in the ground state is π instead of 0. This effect was experimentally demonstrated in early 2000s in the F thickness dependence of the critical current I_c and superconducting critical temperature T_c [64] [66] [65]. Additionally, a dominant second harmonic in the current-phase relation has been observed as half-integer Shapiro steps [67] and magnetic interference patterns with half the expected period [68]. Furthermore, spin-triplet pairing can occur by introducing magnetic non-collinearity at the S/F interface, such as spin-mixer layers [66][10]. The phenomenology of ferromagnetic junctions is very rich and

they have been proposed for numerous applications from superconducting spintronics for the spin-triplet current generation [11] and to phase shifters [69][70]. These applications are based on the long-range proximity effect, which is one of the unconventional phenomena that occurs when a ferromagnet with a non-homogeneous magnetization is employed. The non-homogeneous magnetization gives rise to a spin-mixing and spin-rotation process that generate a triplet component ($S = 1$, $S_Z = 0, \pm 1$).This component is not destroyed by the exchange field in the ferromagnet; rather, it can propagate inside the barrier over distances comparable to the coherence length in normal metals[71].

In this thesis work, the focus is centered in exploiting the memory properties of these junctions for the development of a quantum hybrid circuit. Therefore, it is of fundamental importance understanding their behavior in the presence of a magnetic field. In JJs containing a F barrier, to evaluate the total magnetic flux through the junction Φ, the flux Φ_F due to the F magnetization M_F must be considered: $\Phi_F = \mu_0 M_F L d_F$, where L is the cross-section width of the JJ and d_F is the F thickness [72]. The total flux is thus given by $\Phi_F = \mu_0 H L d_m + \mu_0 M_F L d_F$, where $d_m = 2\lambda_L + d_F$ represents the thickness of the material penetrated by the applied field. Due to the magnetic hysteresis of the F layer, the critical current (I_C) versus magnetic field ($\vec{H}$) curves exhibit an hysteresis, depending on the sweeping direction of $\vec{H}$. When sweeping $\vec{H}$ from positive to negative fields (down curve), the Fraunhofer-like pattern shifts to a negative field due to the positive remanence of the ferromagnet. Conversely, when sweeping from positive to negative fields (up curve), the pattern shifts to a positive field. In the simplest case of a homogeneous F barrier in a single-domain state, we assume that $\mu_0 M_F = \mu_0 M_s \approx \mu_0 M_r$ (where M_s is the saturation magnetization and M_r is the remanent magnetization). The Fraunhofer pattern thus shows simply an offset [73]:

$$\pm\mu_0 H_{shift} = \frac{\mp\mu_0 M_s d_F}{d_m}. \tag{2.13}$$

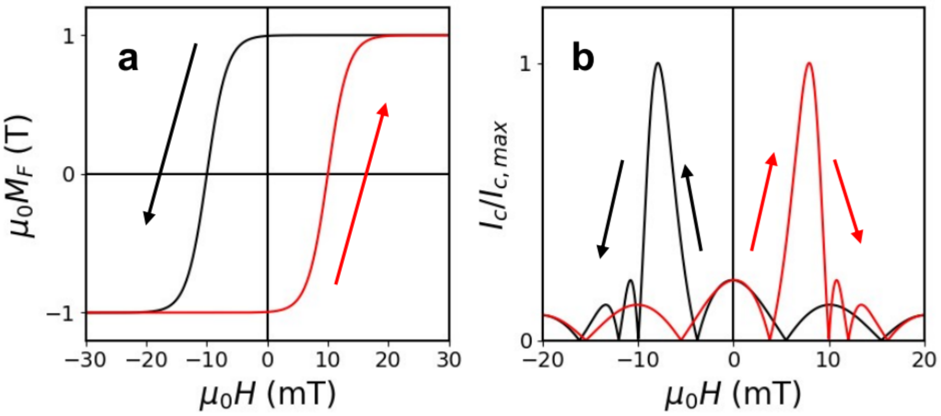

Figure 2.9: a) Hysteretic magnetization loop and corresponding b) $I_C(H)$ curve for an SFS JJ: for down curve (black curve) the Fraunhofer-like pattern shifts to a negative field due to positive remanence of the ferromagnet. For the up curve (red curve), the pattern shifts to a positive field.

Analyzing $I_C(H)$ curves reveals information about the F barrier's magnetization process [72]. For example, in the case of a rectangular junction, in which the $I_C(H)$ curve shows a Fraunhofer pattern described by equation 1.23, the critical current exhibits minima at specific Φ values:

$$\begin{cases} \Phi_{min} = \Phi_0 m, \\ \Phi_{max} = \Phi_0(n + 1/2), \end{cases} \tag{2.14}$$

where m and n are integers. Using these relations it is possible to transform $I_C(H)$ into $\Phi(H)$ dependence, and then into M(H). This method is known as Josephson magnetometry [72].
Due to magnetic hysteresis of the $I_c(H)$ curves, ferromagnetic junctions have been proposed as memory elements for superconducting electronics[74]: by setting a magnetic field, ferromagnetic junctions can realize two states, one with a higher critical current I_c^{High}, corresponding to logical '0', and the other with a lower critical current state I_c^{low}, corresponding to logical '1'. If the initial state is '0', a positive magnetic field pulse can switch the memory to the '1' state. Along the rising edge of the pulse, the critical current moves along the up-curve, for the falling edge of the pulse, the critical current follows the down curves. Along the falling edge of the pulse, the opposite holds [71][72][75]. In the next sections, we will show that the memory properties of MJJs can provide an alternative tuning of the qubit.

2.2 SIsFS JJs

A SIsFS junction consists of two superconducting electrodes separated by a complex multilayer including a tunnel barrier I, an intermediate superconducting s and ferromagnetic F film [75], as schematized in figure 2.10. A standard SFS junction operates in an overdamped regime due to the ferromagnetic nature of the F barrier. By a careful choice of materials and thicknesses, the SIsFS geometry allows to engineer ferromagnetic JJs characterized by high quality factors and underdamped behavior, while preserving the memory properties of a standard SFS. Indeed, the SIsFS structures have been introduced in order to obtain memory elements compatible with $I_c R_N$ product [76][77] of standard superconducting electronics [13][74].

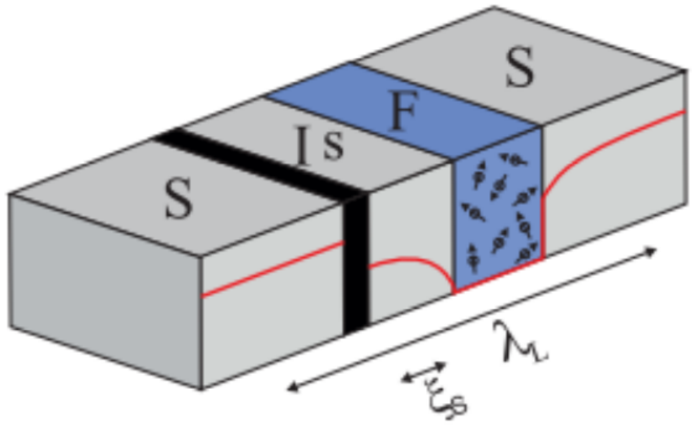

Figure 2.10: SIsFS junction. The red line shows the distribution of pair potential across the structure: it reaches bulk values in both S-electrodes, it is suppressed in the superconducting interlayer s and vanishes in the ferromagnetic layer. The London penetration length λ_L and the coherence length of the superconductor ξ_S are reported.

The Josephson effect in SIsFS junctions in the dirt limit can be described by solving the Usadel equations and by applying the Kupriyanov-Lukichev boundary conditions at Is, sF, and FS interfaces [75]. Similarly to what was done for the S/N interfaces, parameters are defined for the characterization of the interfaces: $\gamma_{BI} = \frac{R_{BI} A_B}{\rho_s \xi_s}$, where R_{BI} and A_B are the resistance and area of the SI interface.

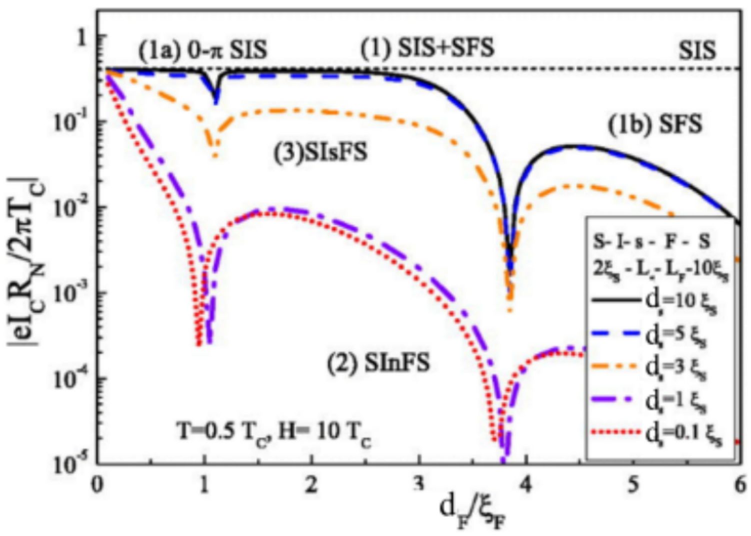

Figure 2.11: Characteristic voltage ($I_C R_N$) behavior in SIsFS structures as a function of the ferromagnetic layer thickness d_F for different superconducting interlayer thicknesses d_s at a temperature of T=0.5T_c. Both thicknesses d_s and d_F are normalized with respect to their coherence length ξ_s and ξ_F, respectively. The dashed black line represents the behavior of the $I_C R_N$ product for a conventional tunnel SIS JJ. At the sF and FS interfaces: $\gamma_{BI} = 1000$,$\gamma_{BFS} = 0.3$, $\gamma = 1$ [75]

Figure 2.11 illustrates how the $I_C R_N$ product varies with the ratio of d_s and d_F with respect to their respective coherence lengths. Different operating modes emerge based on material choices and layer thicknesses. By comparing d_s with the critical thickness d_{sc}, which represents the minimal s-layer thickness in an sF bilayer above which superconductivity persists at a given temperature, distinct transport regimes arise [78]:

- **Mode 1** ($d_s > d_{sc}$): The SIsFS structure acts as a series connection of a tunnel SIs JJ and a ferromagnetic sFS junction. **(a)** For small d_F and $I_{C,SIs} > I_{C,sFS}$, the characteristic voltage resembles a standard SIS junction. The ground state phase difference φ is controlled by the sFS part, allowing for 0- or $\pi-$ ground states. **(b)** At high d_F, the structure behaves as a standard SFS junction.

- **Mode 2** ($d_s < d_{sc}$): Absence of superconductivity in the s-electrode leads to a complex -InF- weak junction region and value of the critical current of the order of SIFS JJs [78][79]. The dependence on d_s is weak due to the large decay length in the n-region with suppressed superconductivity.

- **Mode 3**($d_s \approx d_{sc} \sim 3\xi_s$): the structure's properties are highly sensitive to the ferromagnetic layer's thickness and exchange field, which control superconductivity suppression in the sF bilayer. The latter tune the effective transition temperature T^*, which is the transition temperature of the bilayer sF, causing the appearance of the proximity-like tail observed in temperature dependence of the $I_c R_N$ as shown in Figure 2.12.

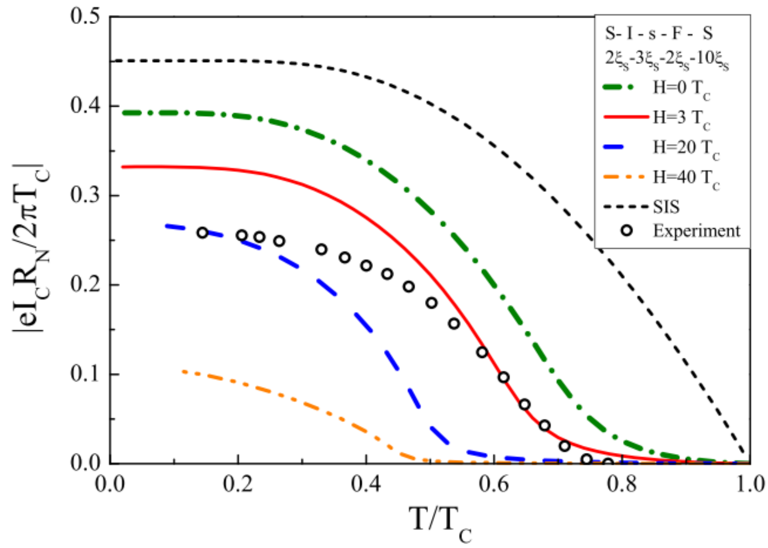

Figure 2.12: Temperature dependence of the characteristic voltage of SIsFS structures at different exchange field values in the F-layer. The short-dashed line represents the behavior typical of a conventional tunnel SIS junction. Notably, the exchange field shifts the effective critical temperature, corresponding to the transition of the sF bilayer into the normal state. Experimental measurements in $Nb{-}Al/AlO_x{-}Nb{-}Pd_{0.99}Fe_{0.01}{-}Nb$ junctions confirm the existence of this effective critical temperature in these samples [82].

Moreover, $d_s < \lambda_L$, the whole structure still behaves as a single junction with respect to an external magnetic field H, since d_s is too thin to screen the magnetic field. When the SIsFS junction is in mode (1a) and far from the 0 - π transition, the current-phase relation has a standard sinusoidal form (Equation 1.8). Thus, in a rectangular JJs we still observe a Fraunhofer-like dependence of the $I_c(H)$ curves. In this case, the total magnetic flux through the junction becomes [75][78]:

$$\Phi = \mu_0 M_F L d_F + \mu_0 H L d_m, \tag{2.15}$$

where the thickness of the material penetrated by the applied field is $d_m = 2\lambda_L + d_s + d_F + d_I$. This layout with $d_s > d_{sc}$ and for $d_s < \lambda_L$ allows for the creation of switchable elements with high quality factors and low dissipation for digital and quantum electronics [13][80][81].

2.3 Ferrotransmon

Superconducting quantum circuits have almost exclusively relied on aluminum-aluminum oxide-aluminum (Al/AlO_x/Al) tunnel superconductor superconductor (SIS) Josephson junctions (JJs) [6] [83]. Exciting phenomena and functionalities can be accessed by exploiting unconventional superconducting systems. This goes beyond merely searching for the best qubit candidate; it's also an advancement toward a better understanding and control of Josephson-based quantum circuits. These devices enhance the capabilities of superconducting electronics and deepen our understanding of exotic phenomena that can arise in hybrid unconventional superconducting devices. For instance, in the specific case of tunable transmon qubits, which typically use external flux fields to change the qubit frequency, hybrid superconductor-semiconductor structures have been employed to enable voltage-tunable transmons (also known as gatemons [84][85]). For what concerns magnetic Josephson junctions, so far they have been used as phase shifters in digital and quantum superconducting circuits [66][10][86]. However, they haven't been considered as active elements for quantum circuits due to their inherent high quasiparticle dissipation. This dissipation arises from the metallic nature of standard ferromagnetic barriers, which negatively impacts the qubit performance. Recent advancements have changed this landscape. By coupling ferromagnetic layers with insulating barriers inside the JJ (SIsFS or SIFS JJs [14]) and leveraging intrinsic insulating ferromagnetic materials (SI_FS JJs), it's possible to engineer ferromagnetic JJs with high quality factors and low quasiparticle dissipation.

These tunnel-SFS JJs thus offer additional functionalities not only in superconducting classical circuits but also in quantum architectures. Recently, it has been proposed to integrate a tunnel magnetic Josephson Junction into a transmon circuit to allow a tuning of the qubit frequency by means of magnetic field pulses, in the so-called ferrotransmon architecture [7].

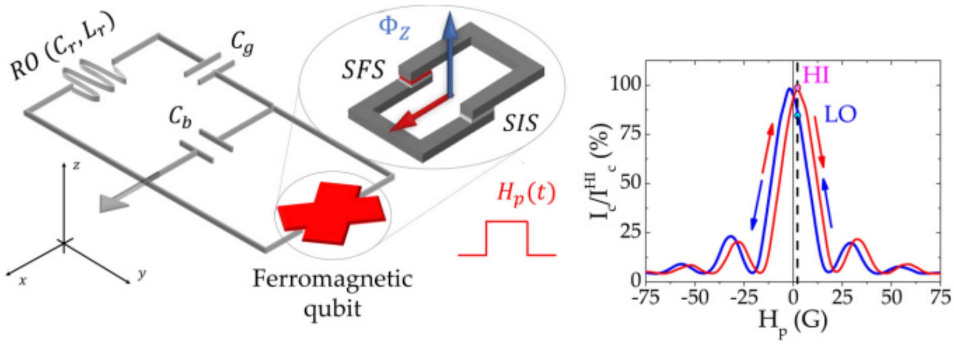

(a) (b)

Figure 2.13: In (a), ferro-transmon circuit design: the readout (RO) resonator is capacitively coupled to the qubit through C_g. The qubit is schematized as a hybrid SQUID in parallel with a bias capacitor C_b. In the SQUID, there are a standard tunnel SIS JJ and a tunnel ferromagnetic SFS JJ. Blue and red arrows indicate magnetic fields applied along the z-axis and the x-axis, respectively. In (b), Ic (H) modulation in a tunnel SIfS JJ. Blue and red curves in (b) refer to the down and up magnetic field pattern, respectively. We highlight in each plot the low- and high-Ic level states (LO and HI) and the working point (dashed black line).

The main idea behind the ferrotransmon, schematized in the figure 2.13, is to achieve digital tuning of the qubit by exploiting the memory properties of a tunnel-SFS JJ into the SQUID loop of a transmon circuit. The SQUID set-up allows a tuning of the qubit frequency as previosly illustrated by applying a flux Φ_z along the z-axis as shown in Fig. 1.15.a. Additionally, as shown in the previous sections, pulsed magnetic fields allow switching between discrete critical current values (LO and HI states) 2.13, thus allowing the tuning of the Josephson energy between discrete values, by applying a magnetic field along the x-axis. Before the pulse, the I_C is in the high-level (HI) state. At the end of the pulse, I_C transitions to the low-level (LO) state.

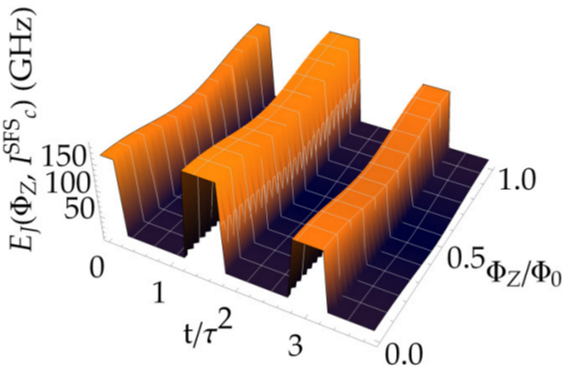

Figure 2.14: Calculated total Josephson energy E_J of a hybrid SQUID composed of a SIS JJ with E_{SIS} J = 10 GHz, i.e., $I_{SISc} \sim 30nA$, and a SIfS JJ with GdN barrier. I_{SFSc} is the critical current of the SFS JJ in the hybrid SQUID,which is fixed here to 350 nA. The 3D-plot shows the dependence of EJ on an external flux Φ_Z (in units of the quantum magnetic flux Φ_0 and the magnetic field pulsed sequence Hp(t) in (c), with time t normalized to τ.

In this configuration, the Josephson energy can be thus tuned exploiting the dependence on Φ_Z and Φ_L:

$$E_J(\Phi_Z, \Phi_L) = E_J\Sigma(\Phi_Z)cos(\pi\Phi_Z\Phi_0) \times \sqrt{1 + d^2(\Phi_L)tan^2(\pi\Phi_Z\Phi_0)} \tag{2.16}$$

where we set $E_J\Sigma(\Phi_Z) = E_J^{SIS} + E_J^{SFS}(\Phi_L)$ and we denote as $d(\Phi_L)$ the asymmetry parameter:

$$d(\Phi_L) = \frac{E_J^{SIS} - E_J^{SFS}(\Phi_L)}{E_J^{SIS} + E_J^{SFS}(\Phi_L)}. \tag{2.17}$$

The asymmetry of the SQUID (parameter d) plays a crucial role. In the simulation in Figure 2.14, the SQUID's JJs have critical currents with a 10-fold difference: $I_{CSFS} \sim 350$nA (dilution temperatures) and $I_{CSIS} \sim 30$nA. Far from the sweet spots, multiple semi-integers of Φ_0, the flux-noise sensitivity of the transmon qubit is significantly reduced. The preference for working with SIsFS junctions over those utilising insulating ferromagnets [66][87] is based on the the larger availability of metallic ferromagnets, which can allow for the engineering of ad hoc hysteresis cycles. The critical current I_{SFS} of the tunnel-SFS junction, along with its tuning via a local pulsed magnetic field ϕ_L, determines the ratio E_J/E_C and the qubit frequency Ω_{01}. Specifically, $\Omega_{01}(\phi_Z\phi_L)$ is given by:

$$\Omega_{01}(\phi_Z\phi_L) = \frac{8E_C}{E_J(\phi_Z\phi_L) - C}, \tag{2.18}$$

where C is the total transmon capacitance. To assess the feasibility of the ferrotransmon and define its circuit design, its electromagnetic response in the two states: HI and LO of the tunnel-SFS JJ has to be characterized. The qubit-readout coupling g for the first two energy levels of the transmon is given by:

$$g = g_{01} = \frac{e}{\hbar}\sqrt{\frac{C_g}{C}}\sqrt{\frac{\hbar\omega_{bare,RO}}{8E_c}}, \tag{2.19}$$

where C_g represents the coupling capacitance and $\Omega_{bare,RO}$ is the bare-resonator frequency. In conventional transmon circuits based on Al or Nb technology, the qubit frequency ω_{01} typically remains below 10 GHz [48]. This frequency range allows easy detection using standard qubit measurement equipment. Charging energies exceeding approximately 200 MHz ensure significant anharmonicity, effectively isolating a quantum two-level system[51][88][89]. In [7], a comprehensive analysis of the aforementioned parameters is conducted, by considering two layouts one with a hybrid DC-SQUID and one with a single tunnel-SFS JJ. The analysis suggests the following ranges of values for the tunnel SFS critical current in order to guarantee the transmon read-out, and suitable frequency and anharmonicity values:

- For the hybrid DC-SQUID configuration, I_{SFSc} ranges from 40 to 65 nA, by settimg E_C is set at 260 MHz (with $C_g = 4fF$ and the bias capacitor $C_b = 70fF$) and I_{SISc} at 30 nA.
- For the single tunnel-SFS JJ layout I_{SFSc} ranges from 25 to 80 nA, by assuming E_C =200 MHz (with $C_g = 4fF$ and $C_b = 90fF$).

In the hybrid DC-SQUID configuration, similar to typical flux-tunable transmons, the tuning extends up to 1 GHz. For a single tunnel-SFS JJ, the frequency shift ($\Delta\omega_{01}$) is approximately 0.8 GHz. For a single tunnel-SFS JJ the tuning of the qubit frequency is dependent on the magnetic pulsed field alone and this tunability corresponds to a current variation (ΔI) of around 30%, achievable even by by engineering the F-barrier. Most importantly, by employing asymmetric minor loops or rectangular MJJs [90], it is possible to engineer MJJs with finite ΔI_c at zero field, thus avoiding the application of a static field that can be detrimental for qubit operations. This means that instead of a hybrid SQUID in the qubit, it may be worth to explore the layout in wihich a single tunnel-SFS JJ is used, thus completely removing the effect of additional flux-noise fluctuations and improving the scalability of the entire quantum circuit.

Chapter 3

Experimental set-up

In this chapter the measurement setup employed to study transport properties of tunnel ferromagnetic Josepshon junctions down to a temperature of about 10 mK will be described. In particular, the cooling system and the electronic setup will be illustrated. In particular, we will give an overview of the techniques used to perform DC- measurements, a brief description of the fabrication procedure and the ANSYS HFSS software used to carry out the electromagnetic simulations of more advanced superconducting circuits.

3.1 Cooling system

The realization of cryogenic systems that presente ^3He-^4He mixtures were first suggested by H.London in 1951[91]. The operation of dilution cryostats is based on the behavior of the ^3He-^4He mixture in the liquid phase, whose phase diagram is shown in the figure 3.1.

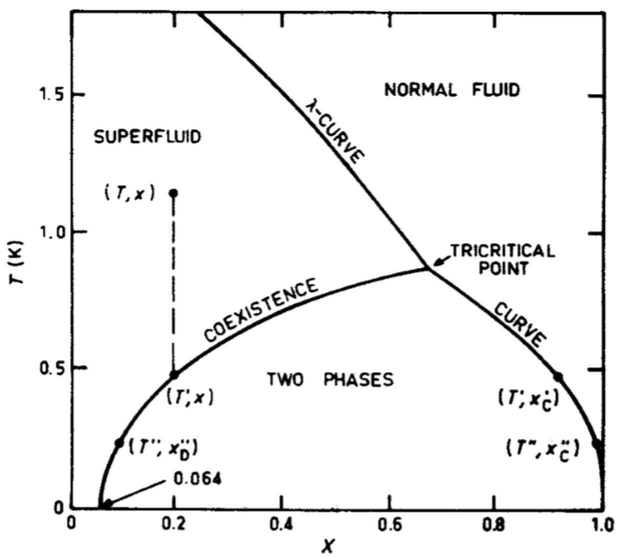

Figure 3.1: Phase diagram of the $^3He/^4He$ mixture. $x = n_3/(n_3 + n_4)$ is the molar concentration of ^3He.

Above the coexistence curve ($T > 0.86K$), the mixture appears in the form of a homogeneous mixture of ^3He dissolved in ^4He. The latter can be either in the normal or superfluid state, depending on the molar concentration of ^3He. When, at a given concentration, the temperature is lowered below the coexistence curve (T,x $\rightarrow$ T',x), the mixture spontaneously separates into two phases: one rich in ^3He (T',xc') lighter and the denser one, rich in ^4He (T',x). The lighter ^3He "floats" on the ^3He-^4He mixture; in order to cool the diluted ^3He it is necessary to subtract it from the ^3He region, by using an external pumping rack. The ^4He has a vapor pressure that is too low to be aspirated and therefore only the ^3He evaporates. This process causes the ^3He to cool, decreasing the temperature of the entire system. The process by which a richer and a poorer region of ^3He is obtained differs in the two types of dilution cryostats: *wet* and *dry*. In this thesis work, a *dry* cryostat, the *Triton*, was used for the characterization of the measurement samples. Dry dilution fridges do not require cryogenic liquids. A sketch of the cryogneic apparatus is schematized in the figure 3.2.

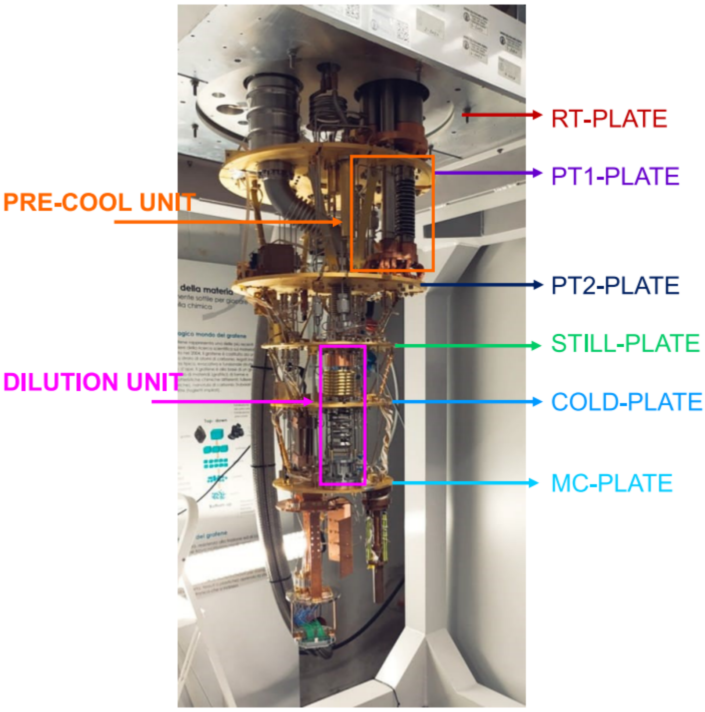

Figure 3.2: Triton inner view where the different components are indicated:

- the RT-plate, at room temperature;
- the PT1, at $\sim$ 70 K;
- the PT2, at $\sim$ 4.2 K;
- the still-plate, at $\sim$ 0.7 K ;
- the IAP-plate, or cold-plate, at $\sim$ 0.1 K;
- the MC-plate, at $\sim$ 10 mK, which has a mixing chamber where the $3^{H}e$ dilution process takes place.

To isolate the cryostat, an outer vacuum chamber (OVC) is present and the vacuum is achieved, by means of an external pump, at a pressure of about $10^{-3} mbar$. The *mixing chamber* is connected to the *still chamber*. In the latter the ^3He is distilled from the *mixing chamber* and flows towards the pumping lines. Moreover, the *cool−down* process is automatic and regulated by softwares. On the *still chamber* plate there is a *heater* to regulate the temperature: in fact, if this dropped rapidly the vapor pressure would be so low as to interrupt circulation. It is also necessary to maintain the temperature of the *heater* in a given range: an excessive power of the *heater* would lead to an increase in the vapor pressure of the isotope ^4He which would decrease the dilution efficiency. An optimal temperature is estimated between 0.7-0.8K. The compressor that replaces the helium bath generates a large amount of mechanical vibrations; to attenuate them, copper braids were added which decouple the compressor from the plates, a detail of which is shown in the figure 3.3:

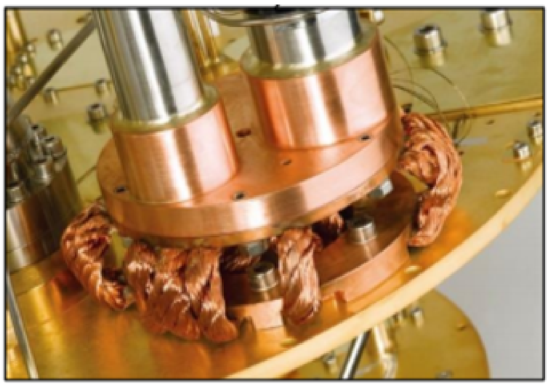

Figure 3.3: Combination of braids and a very rigid support allows vibrations to be reduced, down to the order of the micron.

3.2 Noise Filtering Systems

The study of the transport properties of junctions can be affected by noise sources due to mechanical vibrations, caused by cryostat pumping systems, and by both thermal and electromagnetic noise caused by electronic instrumentation. The attenuation of noise sources due to mechanical vibrations is obtained thanks to the copper braids described in the previous paragraph. As for electromagnetic noise, it is necessary to appropriately filter the dc lines employed for transport measurements of the superconducting samples. The filtering system to reduce the electromagnetic noise is made up of two stages of filters, both for voltage and current lines. The first stage is represented by low-pass RC filters with a cutoff frequency of approximately 1MHz. Such filters lose attenuation at higher frequencies, especially above a few GHz, so another filtering stage is required. The second stage is composed of copper powder (CP) filters which filter the signal by exploiting the oxidation of the copper grains present inside them. In the Triton the CPs are located on the cold palet, at about 100 mK. Furthermore, there is also a system of shields that protect the samples from the external magnetic field and is made up of two screens: an external one, the 1 mm thick cryoperm screen; an internal one of lead 1 mm thick.

3.3 Electronic setup

The measurement setup is designed for four-contact measurements, using one pair of electrodes for the current bias of the junction and the other pair for reading the voltage. It is an advantageous technique compared to a two-contact measurement, in fact it excludes the voltage drop due to the impedance of the filters which would add to the voltage drop across the junction. The two voltage lines V−and V+ are connected to a differential amplifier, with gain varying between 10 and 500, whose output signal is monitored through an oscilloscope. The study of the transport properties of a superconducting device takes place using voltage-current (I-V) characteristics at various temperatures. A low-frequency triangular signal, $\sim 11Hz$ connected to a variable resistor R$_{shunt}$, allows the superconducting device to be current-biased. The bias current I_{mis} is given by the relation:

$$I_{bias} = \frac{V_{pp}}{R_{shunt} + R_{line} + R_{junction}} \sim \frac{V_{pp}}{R_{shunt}}, \tag{3.1}$$

with a peak-to-peak V_{pp} amplitude that falls on the variable shunt resistance R_{shunt}, which is much higher than the resistance of the lines (R_{line}) and the resistance of the junction ($R_{junction}$). The error on the generated voltage is at least of the order of $0.1 - 0.5\%$. The block diagram of the experimental apparatus is shown in figure 3.4.

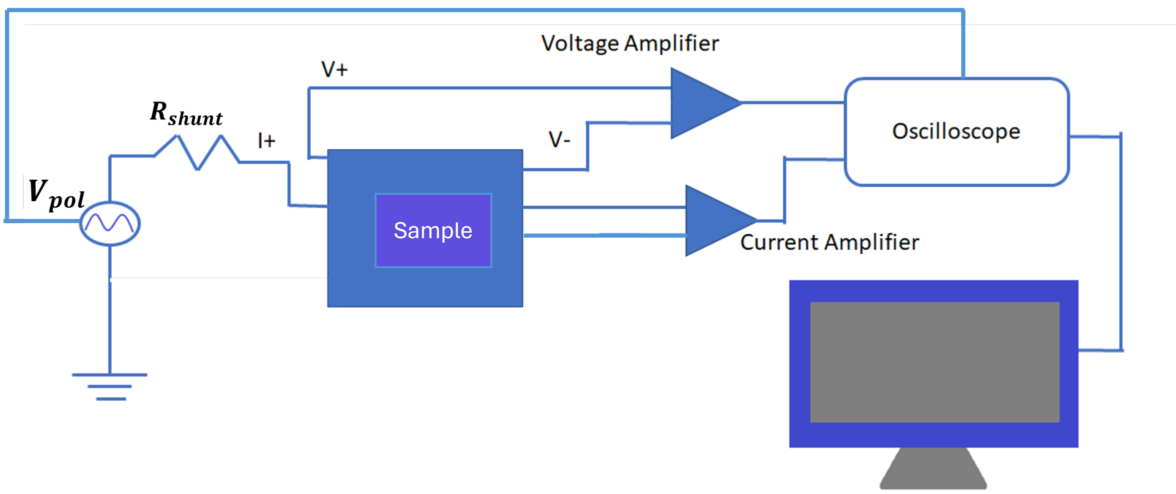

Figure 3.4: Scheme of the measurement setup; the junction is current biased; the current I$_{pol}$ is generated by V_{pol}/R_{shunt}, where Vpol is a triangular waveform($\sim 11Hz$); voltage and current amplifiers are connected to the junction and their outputs are connected to the oscilloscope.

To attenuate the noise due to the electrical network, the amplifiers and the electronic instruments are decoupled from the common ground. The first are powered by batteries, the second are connected to an isolator. The temperature is read on a diode thermometer having low temperature sensitivity of about 1×10^{-4}K; the temperature error is difficult to estimate and varies depending on the interval considered. However, it is possible to obtain good thermalization of the system through the efficiency of the filtering system and the thermal angles placed at the various stages of the cryostat. The I-V characteristic curves associated with the junction transport measurements present a noise band of thermal and electromagnetic origin. The Figure 3.5 shows a zoom of the noise band at zero voltage measured on a superconducting nanostructure taken as reference.

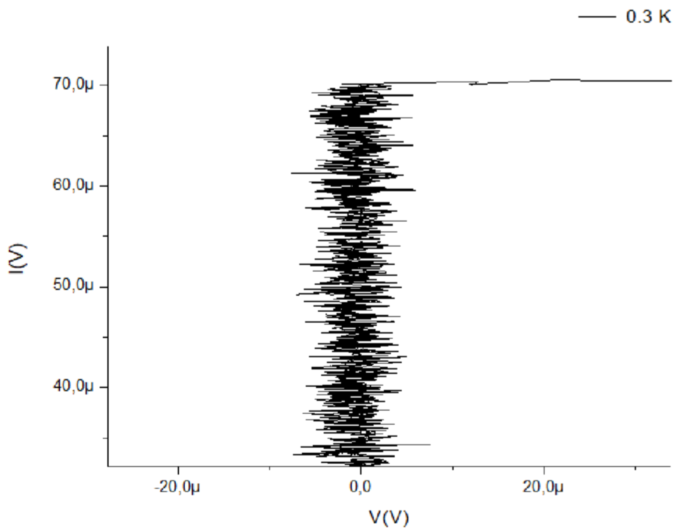

Figure 3.5: Zoom of the I-V characteristic for the Al nanowire to 0.3K: noise band of the zero voltage state

The width $\Delta V = 7\mu V$. Having called V the measurement interval of the potential, we can give an estimate of the relative error in percentage from the ratio $\Delta V/V = 1\%$. This relative error is associated with the measurement of I_c.

3.3.1 Measurements in presence of an external magnetic field

For measurements in presence of an external magnetic field, it is used the Source Meter Keithley 2400 as a current generator. It's connected to a superconducting coil made of N_bT_i. The coil is mechanically anchored to the mixing chamber of the Triton dilution fridge. The current through the coil has a current-to-magnetic field conversion factor of 0.1 T/A. The error on the generated current is specified as $0,5\%$ of the coil current. Initially, a magnetic field is applied from zero to an upper value (virgin curve), then the field is applied from a positive value to a negative value (down curves) and back again (up curves). For each magnetic field value, IV characteristics are acquired. The step size for the coil current (ΔI_{coil}) and the waiting time between acquisitions, t_w are chosen for accurate measurements, $t_w = 1s$. The average of 20 sweeps is taken. The Source Meter Keithley

2400 is remotely connected to a PC via a GPIB (General Purpose Interface Bus) interface. Measurements can be initiated using LabVIEW programs.

3.4 Fabrication of SIsFS Josephson junctions

This work investigates hybrid aluminium-based tunnel ferromagnetic Jospeshson junctions (SIsFS). The samples were fabricated at the CNR-ISASI in Pozzuoli and at the Physics Department of the University of Naples. These junctions are composed by a multilayer barrier comprising a thin insulating layer (Al/AlO_x) and a strong ferromagnetic layer (Permalloy, $Ni_{80}Fe_{20}$). Permalloy is a strong ferromagnet, commonly employed in the fabrication of small-area JJs, in our case facilitating the realisation of circular SIsFS JJs with a diameter of approximately $4\mu m$. In contrast to other superconducting materials, such as niobium, aluminium is not a non-refractory material. Aluminium was selected for these JJs due to its utilisation in contemporary qubit fabrication. Moreover, it is unable to withstand strong magnetic fields and possesses a relatively low critical temperature. The fabrication of aluminium-based JJs employs a process previously optimised for niobium tunnel junctions, which involves anodisation of the aluminium top layer and the addition of an additional silicon dioxide insulating layer. This process reliably produces high-quality JJs with aluminium electrodes of a size down to $12\mu m^2$, using standard optical lithography. The resulting JJs exhibit Josephson energy values (E_J values) that are suitable for integration into transmon quantum architectures. Furthermore, the process enables the deposition of additional layers, including a ferromagnetic (F) layer, subsequent to the definition of the junction. The magnetic properties of Py (permalloy) remain stable, thereby enabling a further reduction in JJ cross-sections to micrometric and sub-micrometric dimensions. In the course of this thesis work, junctions in which the Permalloy was doped with niobium (Nb) and the soft ferromagnet gadolinium (Gd) were characterised, in order to develop tunnel-ferromagnetic JJs with diluted properties of the F layer.

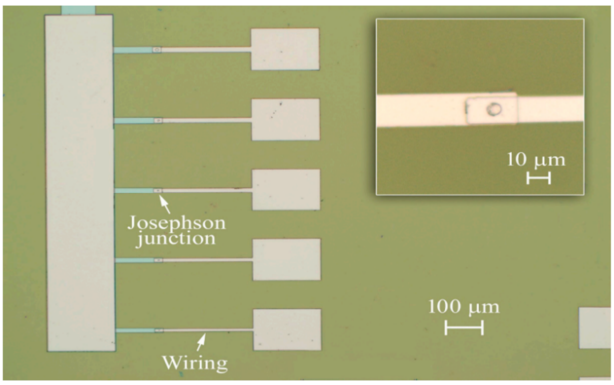

Figure 3.6: Optical microscope image of a set of circular SIsFS with a diameter D ranging from 2 to 10 μm. The inset illustrates the magnication of a circular junction with D = μm.

3.4.1 Codeposition system

For this thesis work, I witnessed part of the sample manufacturing process, in particular that related to thin films deposition process. We primarily employ sputtering to deposit uniform metallic thin films. Sputtering is a kinetic phenomenon where energetic particles – specifically, ionized argon (Ar) atoms – collide with a metallic target material. As a result, a vapor of metallic atoms is ejected onto a nearby substrate. To enhance the deposition rate, we confine the Ar ions using magnetrons, which generate strong magnetic and electric fields. These ions follow helical cyclotron motion along the magnetic field lines, leading to a cascade of ionization events with the surrounding gas. At moderately low pressures (typically below 10^{-2} Torr), sustained plasma forms. Importantly, sputtering maintains the composition of the target material. Whether we sputter a pure element or a compound, the vapor phase remains consistent with the target during deposition. For ferromagnetic materials, the deposition system is composed by three vacuum chambers, each connected by a valve:

- the first chamber is for the etching process; for codeposition, a new technique was adopted which involves the direct passage from the ion etching system to the ferromagnet deposition system, without *breaking the vacuum* using a load lock;

- the second chamber is equipped with two magnetron sources, one of which is an active source. By regulating the power of the magnetrons, it is possible to obtain alloys with a different stoichiometry.;

- the last one contains a single magnetron source for depositing the ferromagnetic materials, in our case the Permalloy (Py). The distance between the target and the sample holder is adjustable, but it has been fixed at 15 cm and the target is placed in front of the substrate to avoid inhomogeneity on the film. As an example, the application of a power of 220 watts resulted in the formation of a layer of Permalloy comprising 10% Niobium;

- the system features a turbomolecular pump (assisted by a rotary pump) to achieve a base pressure of approximately 10^{-7} Torr.

Figure 3.7: Vacuum chamber for the Py deposition and for the ion etching.

3.5 Electromagnetic simulations

Ansys Maxwell is an industry-leading electromagnetic field solver used for designing and analyzing electric machines, transformers, actuators, sensors, and other electromechanical devices. It accurately characterizes nonlinear, transient motion in these components, helping engineers understand their impact on drive circuits and control system design. Ansys Maxwell precisely provides solutions for parameters such as force, torque, capacitance, inductance, resistance, and impedance. By seamlessly integrating with circuit and systems simulation technology, it allows performance evaluation before creating hardware prototypes. Recent innovations in Maxwell have also been developed such as, ECAD-MCAD Integration, Shell Elements Modeling and Resistive Thin Layers Modeling. ECAD-MCAD Integration enables NVH (noise, vibration, and harshness) analysis on complex printed circuit boards (PCBs) by predicting electromagnetic forces and losses for thermal and NVH assessments. Shell Elements Modeling improves the accuracy of electromagnetic field calculations for EMI/EMC (electromagnetic interference/electromagnetic compatibility) and magnetic shielding, helping to optimise designs. In addition, Resistive Thin Layers Modelling improves arcing simulations.
The simulator Ansys HFSS (High-Frequency Structure Simulator) is specifically designed for high-frequency electronic products. It's commonly used for designing antennas, antenna arrays, RF/microwave components, high-speed interconnects, filters, connectors, IC packages, and printed circuit boards. HFSS employs a 3D full-wave solver for RF and high-speed design. While HFSS excels in modeling transmission lines, it cannot directly combine power electronic circuits with geometry models. Additionally, it doesn't directly model power electronics' electrical characteristics using lumped circuit elements or black box representations. For this thesis, Ansys HFSS was employed to simulate the magnetic field and its components generated by aluminium lines of different shapes in a given region

of space. HFSS allowed the investigation of how different shapes and sizes of aluminium lines affect the magnetic behaviour. The simulations are discussed in the fourth chapter and were carried out to investigate the most promising designs for maximising the in-plane field at the junction.

Chapter 4

Experimental results and data analysis

In this chapter, we discuss the key role of tunnel SIsFS JJs and the prerequisites for their on-chip control for the actual implementation of the hybrid ferromagnetic transmon, illustrated in the section 2.3. We first examine the transport properties of a SIsFS JJ with Al electrodes and Permalloy (Py: $Ni_{80}Fe_{20}$) as F layer. We show that these SIsFS JJs exhibit the underdamped behavior of a standard tunnel junction and Josephson energy values suitable for the implementation in the ferrotransmon. However, to demonstrate their switching properties, we have to apply magnetic fields larger than 40 mT, which is unfeasible for the perspective of superconducting quantum architectures. In the second section, we thus discuss our preliminary results on SIsFS JJs employing a diluted NiFe alloy ($Ni_{70}Fe_{11}Gd_3Nb_9$) to reduce the coercive field of the ferromagnetic barrier. We demonstrate that the doping with Gd and Nb enables a reduction of the fields to switch the junction. In contrast to standard flux-tunable transmons, which feature flux-bias lines inductively coupled to d.c. SQUID loops, standard SIsFS JJs require in-plane magnetic field to be switched. Motivated by this issue, at the end of the chapter, we will devote a special focus on the design and simulations of flux line layouts to generate in-plane magnetic fields, fundamental for an on-chip control of the qubit frequencies in the ferrotransmon.

4.1 Characterization of SIS and SIsFS junctions

In this section, we will carried out an analysis of the transport and magnetic properties of SIS and SIsFS junctions.

4.1.1 I-V curves and temperature dependence

So far, SIsFS based on Nb technology have employed soft ferromagnets, such as $Pd_{99}Fe_{01}$, to ensure very small coercive fields [81][92]. However, PdFe alloy are not suitable for the realisation of nanoscale devices, due to the percolative nature of the exchange interaction between iron atoms, which can result in frustrated magnetic properties when reducing the dimensions [93]. As addressed in Ref.

[13], the use of a strong ferromagnet such the permalloy (Py: $Ni_{80}Fe_{20}$) allows to scale SIsFS JJs down to submicron dimensions. However, while Nb serves as the base material for most of conventional superconducting digital circuits, quantum coherence times of Nb-based qubits are significantly shorter than those of their Al-based counterparts [94, 95, 96]. For these reasons, the starting point of our discussion is the investigation of SIsFS JJs with Al electrodes and Py as F barrier.

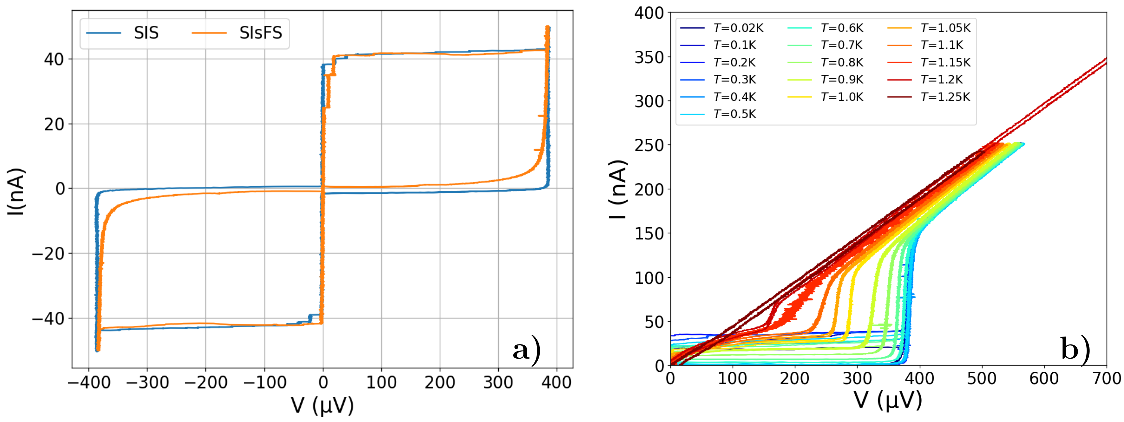

Figure 4.1: **a)** Current-voltage (I-V) characteristic at base temperature 10 mK for a Al (200 nm)/AlO_x/Al (400 nm) SIS junction (blue curve) and for a SIsFS (Al (200 nm)/AlO_x (3 nm)/Al (30 nm)/Py (3 nm)/Al (400 nm)) junction (orange curve). Both junctions have a diameter of $4\mu m$. **b)** I–V curves for a SIsFS junction with a diameter of $4\mu m$ as a function of the temperature T.

The analysis presented here aims at demonstrating that a SIsFS junction can behave as a serial connection of a SIs tunnel junction and a ferromagnetic sFS junction. Through the study of the I-V characteristics, we gain an insight into the transport properties of the junction and of its electrodynamics. The I-V curves of a SIS Al (200 nm)/AlO_x /Al (400 nm) and SIsFS (Al (200 nm)/AlO_x/Al (30 nm)/Py (3 nm)/Al (400 nm)) junction with a diameter of $4\mu m$ are presented in Figure 4.1. The acquisition of I-V characteristics is divided into two datasets, which are intuitively identified as "short range" (Figure 4.1a) and "long range" (Figure 4.1b). The distinction between the two acquisitions lies in the current range. In order to obtain a more precise estimation of the critical current, data close to the expected I_c are recorded in the short range dataset. In the long range dataset, we give a bias current up to the resistive branch to provide an estimation of R_N, as well as the gap voltage V_{gap}. As the switching event to resistive branch is stochastic, we have acquired and averaged 100 I-V curves for each temperature. By comparing the I-V characteristics of a standard SIS and a SIsFS at $T = 10$ mK in Figure 4.1a, it is evident that the presence of the Py interlayer does not affect the transport properties of the measured junctions, since almost the same values of I_c and the shape of the subgap branch of a standard tunnel junctions are observed [97, 98]. Fixing a criterion based on voltage threshold ($V_{th} \sim 50\mu$V), we have estimated the values of the critical current I_c. At $T = 10$ mK, the tunnel

SIsS junction has a critical current density value $J_c = (0.33 \pm 0.07) A/cm^2$, while the ferromagnetic one has $J_c = (0.30 \pm 0.06) A/cm^2$. We have calculated the error bar by propating the errors on the area of the junctions due uncertainties in fabrication process ($\sim$ 10%)[99] and on I_c ($\sim$ 1%), as discussed in section 3.3. Measurements as function of temperature up to T_c ($\sim$ 1.3 K) are reported in in Figure 4.1b. From each curve, the gap voltage $V_{gap} = 2\Delta/e$ (Figure 4.2a) and the $I_c R_N$ product (Figure 4.2b) have been extracted. We have numerically differentiated the I-V curve and estimated the voltage V_{gap} in correspondence with the dI/dV peak voltage. With this method, we have determined a value of V_{gap} of $\sim 400 \mu V$ at $T = 10$ mK. For voltage values that far exceed those of the V_{gap}, we have calculated the normal resistance R_N with an associated error of 3%. We have fitted the experimental temperature dependence $\frac{2\Delta}{e}(T)$ in Figure 4.2a by considering the Bardeen-Cooper-Schrieffer (BCS) relation in the weak coupling limit:

$$\frac{2\Delta}{e}(T) = \frac{2\Delta_0}{e} tanh\left(1.74\sqrt{1 - \frac{T_C}{T}}\right); \tag{4.1}$$

while $I_c R_N(T)$ curves in Figure 4.2b follow the Ambegaokar-Baratoff relation:

$$I_c R_N = \frac{B\pi}{2} \frac{\Delta(T)}{e} tanh\left(\frac{\Delta T}{2k_B T}\right). \tag{4.2}$$

The equation 4.2 differs from the previous Ambegaokar-Baratoff relation 1.16 for the factor B, which is a fitting coefficient that takes into account the suppression with respect to the theoretical value. The observed suppression of I_c enables a return to the transmon regime, with compatible values of E_J, as evidenced in reference [100]. The fits are shown as blue line in Figure 4.2, while Table 4.1 summarises the estimated parameters from Figure 4.2.

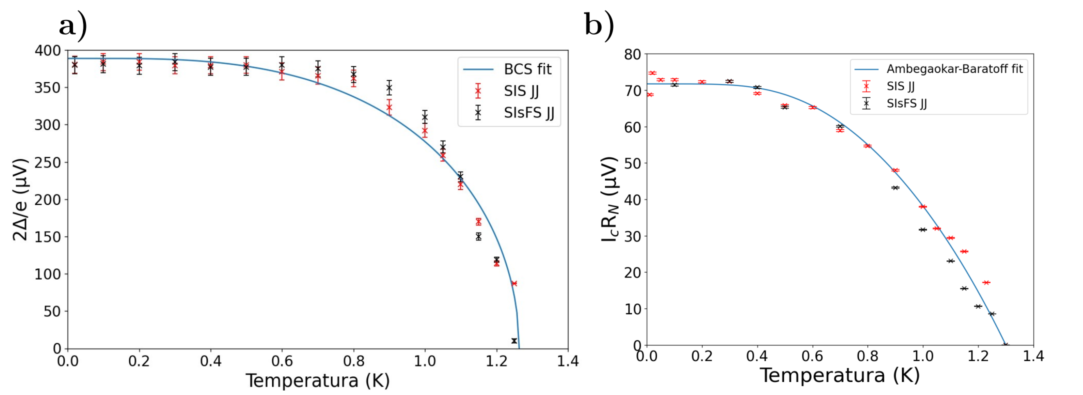

Figure 4.2: **a)** Behaviour of V_{gap} as a function of the temperature: experimental data for a circular SIsS and for a SIsFS are shown as black and red dots, respectively. The blu line is the fitting curve calculated by using the equation 4.1. **b)** Temperature dependence of critical current I_c: black and red dots indicate the experimental data for a circular SIsS and for a SIsFS, respectively. The blue line is the fitting curve calculated by using the equation 4.2. In both the panel, the junction are circular with a diameter of $4\mu m$.

JJs	D (μm)	J_c (A/cm^2)	R_N (kΩ)	I_cR_N (μV)	R_NA ($k\Omega\mu m^2$)	$2\Delta_0$ (μV)	B	T_c K	E_J μeV
SIS	4	0.33 ± 0.07	1.7	68	21.5	388 ± 5	0.33 ± 0.04	1.26 ± 0.05	90.0 ± 0.9
SISFS	4	0.30 ± 0.03	1.7	70	21.5	404 ± 4	0.31 ± 0.02	1.25 ± 0.06	88.5 ± 0.9

Table 4.1: Parameters for the SIS and SIsFS junctions: D represents the diameter of the junction, A denotes the area, J_c is the critical current density, and R_N is the normal resistance estimated at T=10mK. The energy gap at $T = 0$ K Δ_0 and the critical temperature T_c are estimated as fitting parameters from the analysis of the V_{gap} as a function of temperature. The parameter B is introduced to account for the observed suppression of the critical current-normal resistance product I_cR_N in comparison to the Ambegaokar-Baratoff expected value.

From the parameters in Table 4.1, we can conclude that the developed multi-step fabrication procedure allows building magnetic tunnel SIsFS JJs preserving all the features of standard Al tunnel SIS JJs. Most importantly, the Josephson energy value associated with the junction is suitable with the operational parameters of the transmon qubit, as outlined in reference [6], within which the ferrotransmon operates [43].

4.1.2 Josephson magnetic pattern for SIS and SIsFS

As explained in Section 1.2.1, the application of an external magnetic field leads to a diffractive modulation of the critical current of a Josephson junction. An external magnetic field H determines a phase variation in the macroscopic wave function of bulk superconductors, with a thus direct impact on the critical current. Magnetic field measurements are conducted using a current-polarized NbTi superconducting coil, which generates a magnetic field H orthogonal to the junction supercurrent. The I-V characteristics are acquired as a function of the magnetic field, which varies in sweeping ranges of order of mT. The critical current is then estimated for each I-V curve as a function of the applied field, thus reconstructing the magnetic dependence of the critical current.

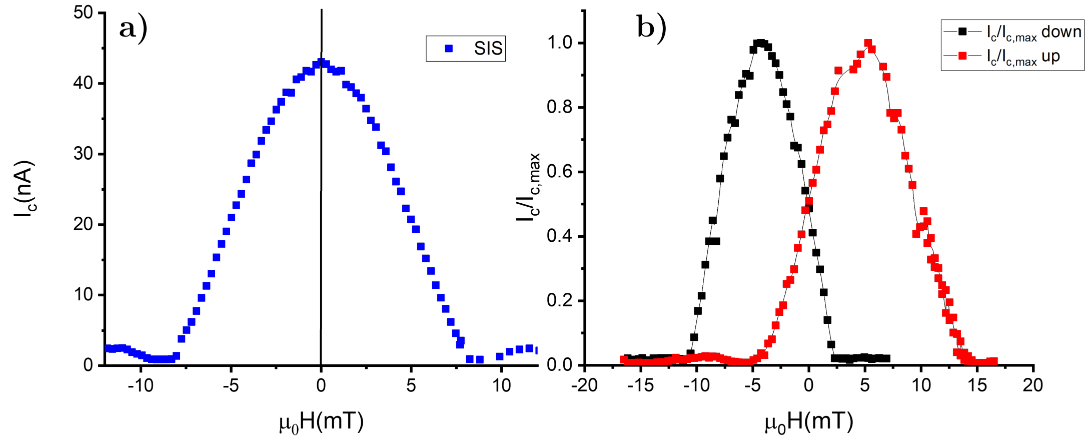

Figure 4.3: **a)** Plot of I_c versus magnetic field H at temperature of 10 mK for the SIS junction exhibits the characteristic Airy diffraction pattern. **b)** The hysteretic behaviour of the $I_c/I_{c,max}$ vs. H curve was acquired by applying a magnetic field in excess of 50 mT. The black and red curves illustrate the magnetic pattern in the down and up direction of the magnet, respectively.

In order to guarantee that a SIsFS junction behaves as a serial connection of a SIs and sFS JJ, but still shows memory properties, the s interlayer has to fulfill the condition $d_s < \lambda_L$ [75]. We can estimate the London penetration length from the SIsS magnetic pattern shown in Figure 4.3a. For circular junctions with the current flowing out-of-plane and the field applied in-plane, I_c follows an Airy pattern in flux with its first minimum at $\Phi = 1.22\Phi_0$, as shown in Figure 1.7. From the minimum of the pattern in Figure 4.3a, we can thus estimate the magnetic thickness d_m of the SIsS JJ. In this case, we have that $d_m = 2\lambda_L + d_I$ with $d_I \approx 1nm$, and the London penetration depth for our aluminium films is thus approximately 35 nm. Therefore, we can conclude that the s interlayer in the SIsFS JJ is smaller than λ_L and we expect that the SIsFS in presence of an external magnetic field operates as a single junction with respect to an external magnetic field H with an hysteretic behaviour of the $I_c(H)$ curves [75]. For circular junctions with the current flowing out-of-plane and the field applied in-plane, I_c follows an Airy pattern in flux with its first minimum at $\Phi = 1.22\Phi_0$, as shown in Figure 1.7. From the minimum of the pattern in Figure 4.3a, we can thus estimate the magnetic thickness d_m of the SIsS JJ. In this case, we have that $d_m = 2\lambda_L + d_I$ with $d_I \approx 1nm$, and the London penetration depth for our aluminium films is thus approximately 35 nm. Therefore, we can conclude that the s interlayer in the SIsFS JJ is smaller than λ_L and we expect that the SIsFS in presence of an external magnetic field operates as a single junction with respect to an external magnetic field H with an hysteretic behaviour of the $I_c(H)$ curves [75].

Upon applying a field of 50 mT, the ferromagnet acquires a remanent magnetization and a shift described by equation 2.13 in the pattern is observed for the SIsFS junction in Figure 4.3b. In order to ensure that the superconductor did not trap flow in the aluminium, we took great care to rise the temperature above the

T_c of the superconductor up to $T = 4$ K, and then lowered the temperature to $T = 10$ mK again to perform the measurements. [53]. The measurements acquired for SIsFS demonstrate that such junctions can be utilised as switching magnetic elements, as evidenced by the cited literature [13][80][82][90]. These findings confirm that the SIsFS JJs can preserve the tunnel behavior of a standard SFS and the memory properties of a SFS, thus suggesting the advantage of integrating these MJJs into quantum architectures.
However, in order to observe a discernible shift in the Fraunhofer pattern, a magnetic field of 50 mT was required. However, this value is extremely hard to handle for the implementation in a quantum circuit, as the requisite current is generated by a coil. In a transmon, this current is typically provided by a bias line inductively coupled. It is also essential to reduce the fields, as the aluminium traps magnetic flux. The following section will examine how optimising the barrier can result in shifts with smaller fields, before presenting alternative flux line designs 3.5.

4.2 Barrier optimization: Permalloy dilution

In the preceding paragraph, the data for a SIsFS with a Permalloy (Ni_{80} Fe_{20}) ferromagnetic layer were presented. Permalloy is a strong ferromagnet that exhibits a considerable exchange energy [101]. The optimization of the Permalloy barrier for the samples presented was achieved through the doping of Permalloy with gadolinium, which couples antiferromagnetically to the ferro-nickel, thus reducing the magnetization. On the other side, the doping of Permalloy with niobium introduces non-magnetic inclusions, thus inducing domains walls motion mechanisms that need smaller fields to be activated [66][102]. These properties reflect in the Fraunhofer patterns. In this section, we present the data for a SIsFS JJs with a ferromagnetic layer with the composition: $Ni_{77}Fe_{11}Gd_3Nb_9$. The same type of analysis illustrated previously was carried out on these ferromagnetic junctions to estimate their transport properties, which are shown in Table 4.2 with the corresponding relative errors.

JJs	D (μm)	J_c (A/cm^2)	R_N (KΩ)	$I_C R_N$ (μV)	E_J (μeV)
SISFS 21 C	4	0.30 ± 0.03	1.80 ± 0.05	95 ± 4	74 ± 2
SISFS 21 D	5	0.33 ± 0.03	2.57 ± 0.08	177 ± 7	119 ± 4

Table 4.2: Parameters of circular SISFS JJs with aluminum electrodes and $Ni_{77}Fe_{11}Gd_3Nb_9$ as F layer a $T = 10$ mK.

The data indicate that the critical current density is comparable with that of tunnel junctions, thereby demonstrating that the SIsFS junction with this dilution of the ferromagnetic barrier still behaves as a series and in the tunnel regime. Furthermore, magnetic field measurements were conducted on these samples, as illustrated in paragraph 4.1.2. We thus present the results of the measurements conducted on a junction with a radius of R=2 μm and sweep ranges of (-25, 25) mT (Figure 4.4a) and (-15, 15) mT (Figure 4.4b).

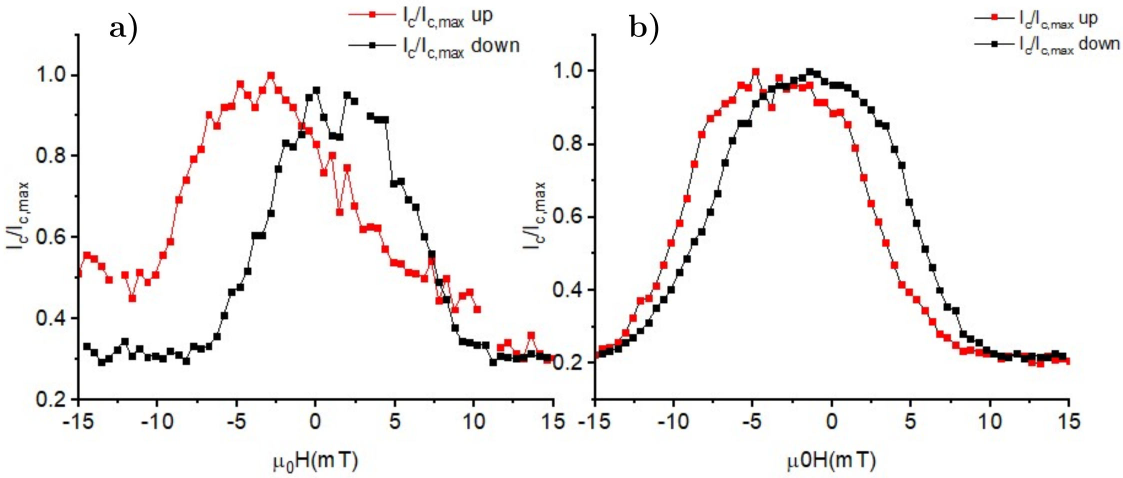

Figure 4.4: Hysteretic behaviour of $I_c/I_{c,max}$ vs. H for a circular SIsFs junction with aluminum electrodes and $Ni_{77}Fe_{11}Gd_3Nb_9$ as F layer a T = 10 mK. The curves were obtained by applying a magnetic field of **a)** 25 mT and **b)** 15 mT. Red curves are obtained by sweeping the magnetic field from positive to negative values, while black curves are obtained by sweeping the field from negative to positive values.

Measurements in the magnetic field were carried out taking into account the current generated to attenuate the electromagnetic noise, using a frequency of 5 Hz. For small currents, the switching is not estimated; the subgap branch is the most sensitive to frequency resolution. A comparison of the $I_c(H)$ presented previously with the current data reveals an inverse hysteresis of the $I_c(H)$ curves in Figure 4.4. This behaviour may be attributed to the inverse proximity effect [57][103], therefore further temperature analyses were conducted as presented in Figure 4.5. The shifts of the magnetic field patterns in Figure 4.5 do not chage by varying the temperature, indicating that the inversion of the up and down curves has to be attributed to demagnetising field effects or to uncertainty on the s layer thickness, which can be slightly larger than λ_L.

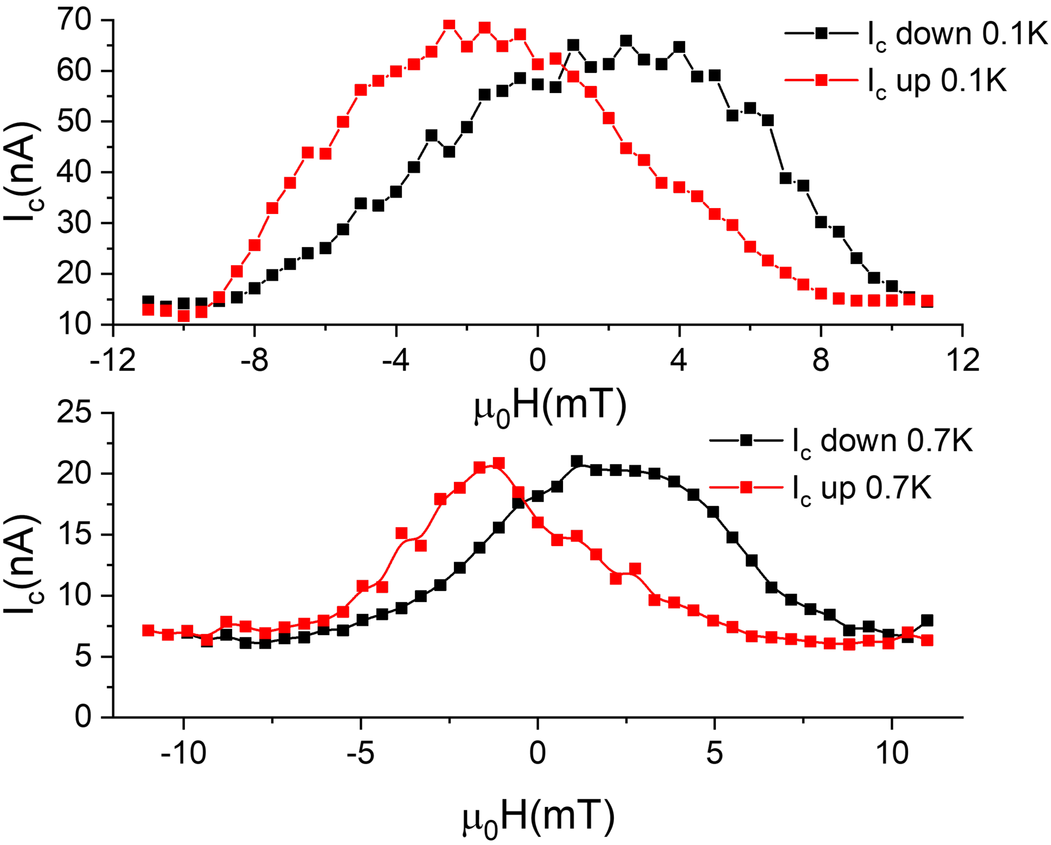

Figure 4.5: Comparison of hysteretic behavior of $I_c/I_{c,max}$ vs. H for a circular SIsFs junction with aluminum electrodes and $Ni_{77}Fe_{11}Gd_3Nb_9$ as F layer a t $T = 10$ mK at different temperatures.

The main result is that a shift in the Airy-like pattern is observed up to fields of -15 to 15 mT, a factor of 3 reduction compared to the ferromagnetic junction with undiluted Permalloy. This suggests that optimising the barrier by diluting the permalloy with gadolinium and niobium is a promising way to achieve on-chip control of the junction.

4.3 Comparative analysis of flux coil designs by Maxwell3D HFSS Ansyss.

So far, the use of coils has not posed limitations in the experimental investigation of our SIsFS JJs. However, in a superconducting quantum processor applying a magnetic field with a coil would simultaneously affect all the qubits. Therefore, each qubit must have a dedicated line for localized tunability. In current qubit architectures, the field tunability is given by the presence of the SQUID, with the bias current generated by a flux line that is inductively coupled to the circuit. In the ferrotransmon, the ferromagnetic junction replaces the SQUID. For implementation of this hybrid quantum circuit, it is essential to consider local tunability on the chip and therefore seek solutions that provide an in-plane magnetic field. The challenge, therefore, is to determine the optimal method for applying the magnetic field to the junction. To determine the extent of the magnetic field that can be applied to the ferromagnetic layer, considering only the in-plane components, we have performed Maxwell3D HFSS of the flux line with a variety of designs. The objective was to achieve the desired magnetisation while simultaneously minimising power dissipation within the chip. In collaboration with Quantumware, a variety of design configurations were explored with the objective of delivering a field pulse and tuning the ferromagnetic layer, with a view to investigating the potential for integration into a quantum circuit. Three distinct designs were subjected to investigation: a superconducting pillar, a CPW (coplanar waveguide), and Helmholtz flux coil. This latter geometry is currently under investigation by Quantware. In the analysis and modeling, a number of factors were taken into account, both in terms of potential nanofabrication and the constraints on the currents that can be employed in the context of circuit implementation, with a view to avoiding thermal effects. All devices are assumed to be made of aluminum, whose critical current density is of the order of $10^6 A/cm^2$. Furthermore, the dimensions of the analyzed designs were also considered in light of this data.

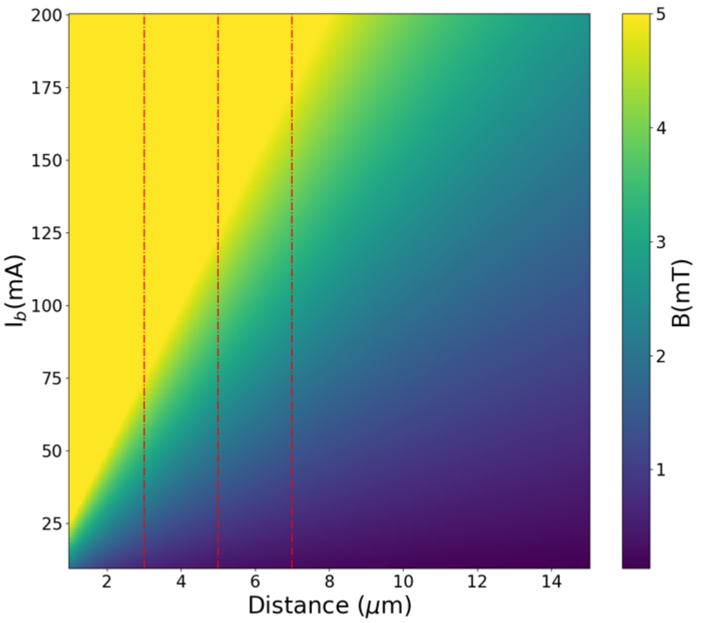

Figure 4.6: Colour map of the magnitude of the magnetic field generated by a superconducting pillar as a function of the bias current and the distance from the surface of the pillar: if the junction with a diameter of $4\mu m$ is placed at a distance of 3 μm from the pillar, it can be seen that currents greater than 100 mA are required to obtain a magnetic field of 5 mT in the middle of the junction.

For the superconducting pillar design, a preliminary color map of the magnitude of the magnetic field generated as a function of bias current and distance 4.6, incorporating the aforementioned limits. The dimensional parameters of the pillar and the distance between the pillar and the ferromagnetic layer were defined according to the constraints imposed by the optical lithography fabrication technique. The ferromagnetic layer has circular symmetry with a radius of $R = 2\mu m$, while the pillar has a radius of $R = 5\mu m$. The distance between the centres is $10\mu m$. Figure 4.7 shows a sketch of the design.

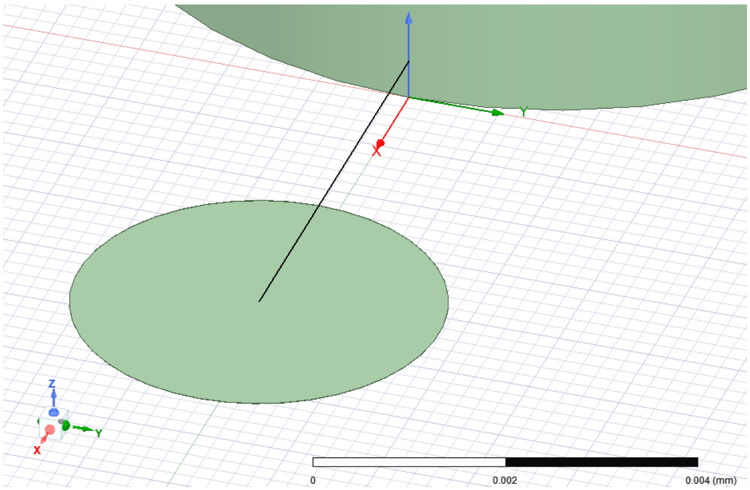

Figure 4.7: Maxwell Ansys 3D design sketch: the ferromagnetic layer with radius $R = 2\mu m$ is placed at a distance of $3\mu m$ from the superconducting pillar with radius $R = 5\mu m$. The distance between the centres is $10\mu m$.

The graph below shows the evolution of the magnetic field as a function of distance as the current varies. Since the simulations are assumed to have in-plane control of the junction, only the y-component of the magnetic field is considered. According to the preliminary analysis of the colour plot, it is possible to achieve a field component of about 5 mT with currents of 200 mA. Although this current is lower than the critical current for aluminium, there is a significant variation in the y-component of the magnetic field along the diameter of the junction, so it is not possible to obtain a homogeneous field. The pillar design, which has the advantage of being dependent only on the radius of the pillar, does not appear to be a promising design unless advanced lithography techniques are employed.

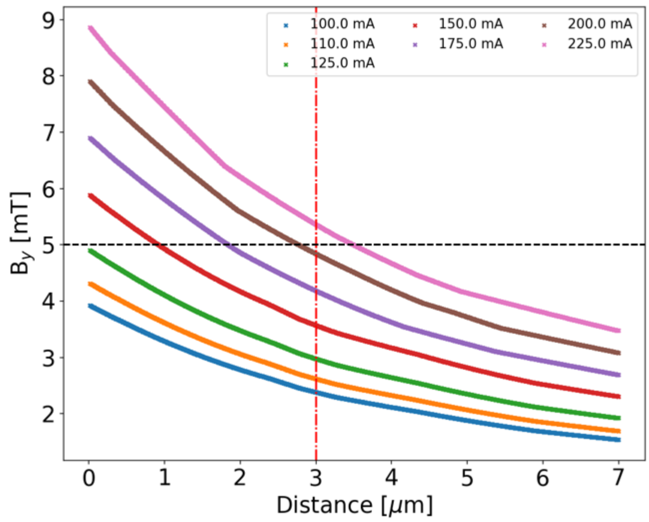

Figure 4.8: The magnetic field trend as a function of distance is reported for a circular junction with a radius of $R = 2\mu m$ and a pillar with a radius of $R = 5\mu m$. The red dotted line indicates the surface of the junction.

An additional design option under consideration is a superconducting CPW flux line (SCPWF) situated beneath the junction. This configuration was employed with the SIsFS junctions for the purpose of creating magnetic memories, with the significant distinction that the CPW also served as the JJ electrode[90]. For our purpose, we should consider to deposit at least a 100 nm insulating layer to prevent galvanic contact between the flux line and the JJ.

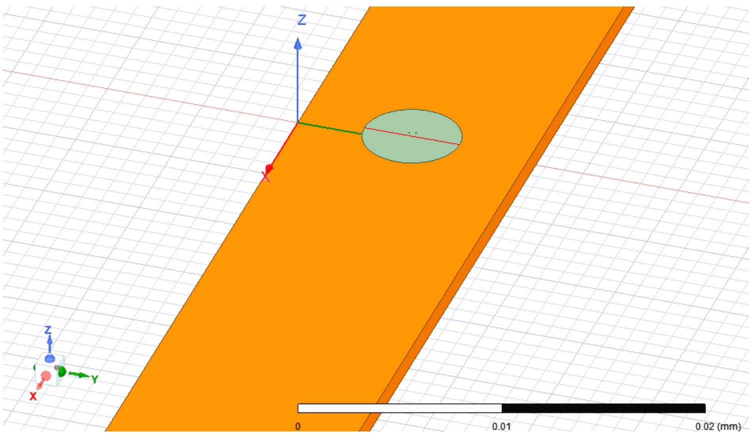

Figure 4.9: Maxwell Ansys 3D design sketch of the SCPW: the ferromagnetic layer is represented as a circular area with a radius of $R = 2\mu m$ and a height of h = 400 nm from the SCPW. The SCPW has a width of $12\mu m$ and a thickness of $1\mu m$.

The ferromagnetic layer is consistently represented as a circular area with a radius of $R = 2\mu m$ and a height of h = 400 nm from the SCPW. This is done to account for the additional layers that constitute the SIsFS junction. The insulating layer, which constitutes the entirety of the junction, serves to preclude galvanic contact coupling. The line has a width of $12\mu m$ and a thickness of $1\mu m$. The width of the SCPW is considerably larger than that of the JJ, and the junction is placed in the centre of the line. This positioning and the proximity of the layer to the line ensures that the magnetic field is uniform within the junction area. Again, only the y-component of the magnetic field is examined.

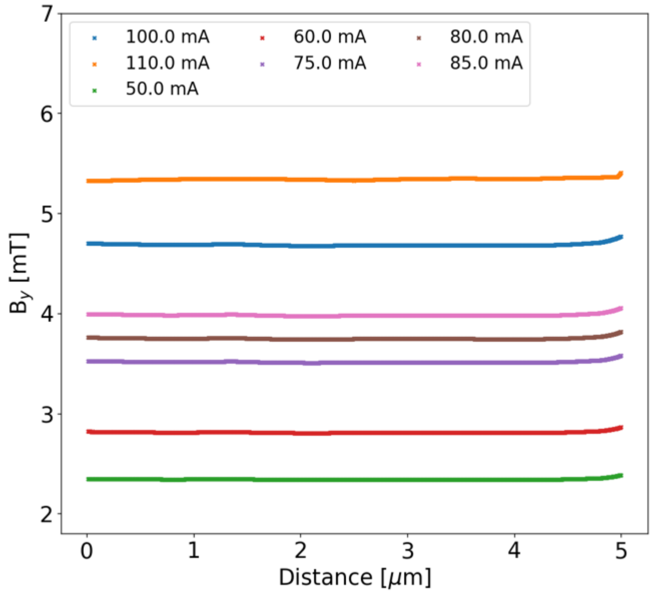

Figure 4.10: The magnetic field trend as a function of distance, calculated for a circular junction with a radius of $R = 2\mu m$, placed at a height of 400 nanometres from the line. The line has a cross-sectional area of $12\mu m$ x$1\mu m$.

The resulting plots, 4.10, show that at a current of range of 100 to 110 mA a magnetic field of about 5mT is reached, which aligns with the typical hysteresis shift observed in SIsFS JJs. It can be observed that the magnetic field is uniform across the entire area, and that proximity effects are not present.

The final design comprises two Helmholtz flux coils [104][105] with 3D spirals on either side of the SIsFS junction (Figure 4.11). This configuration, also known as the Air-Bridge, is currently undergoing analysis by Quantware. The two spirals situated on either side of the junction are positioned in order to generate a strong in-plane magnetic flux. The positioning of a superconducting strip in close proximity to the SIsFS junction may facilitate the connection of the qubit to a high-bandwidth environment, although this could potentially result in a loss of coherence. Nevertheless, the coil design provides a safer alternative. The design is schematised in Figure 4.11, which depicts two connected coils separated by a distance of $10\mu m$. This distance is maintained in order to ensure electrical continuity with the junction between the coils, which are connected under the bridge. Electromagnetic simulations were conducted to examine the impact of loop height on magnetic field generation. The dimensions of the flux lines were fixed at $2.5\mu m$ width and 150 nm in thickness, while the dimensions of the loop were set at $4\mu m$ and a height of $1\mu m$.

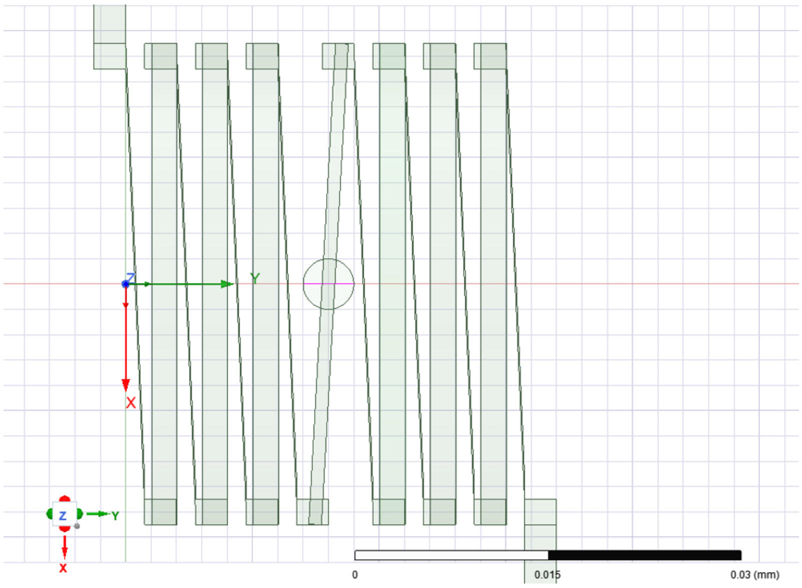

Figure 4.11: Top view of Maxwell Ansys 3D design Air Bridge sketch: the configuration comprises two interconnected coils, with a distance of $10\mu m$ between them. The width of the flux line is $2.5\mu m$ and it has a thickness of 150 nm; the loop presents a width of $4\mu m$ and a height of 1 micrometre. The radius of the ferromagnetic layer is $R = 2.5\mu m$.

Figure 4.12 shows the trend of the component y of the magnetic field along the junction diameter of $5\mu m$. It can be seen that the magnetic field is not uniform, which is confirmed by the simulation of the vector trend of the B-field. This indicates the presence of significant boundary effects due to the geometry of the structure. Two of the bias lines connecting the lateral loops pass very close to the junction, giving an additional contribution to the field. The design considered still respects the manufacturing specifications in terms of the overall length of the structures and the position of the joint relative to them. It should be noted that this design makes it possible to obtain significant magnetic fields with a reduction in bias currents compared to the other two designs studied. Indeed it is possible to generate a field strength of 5 mT at the junction with a current of 50 mA.

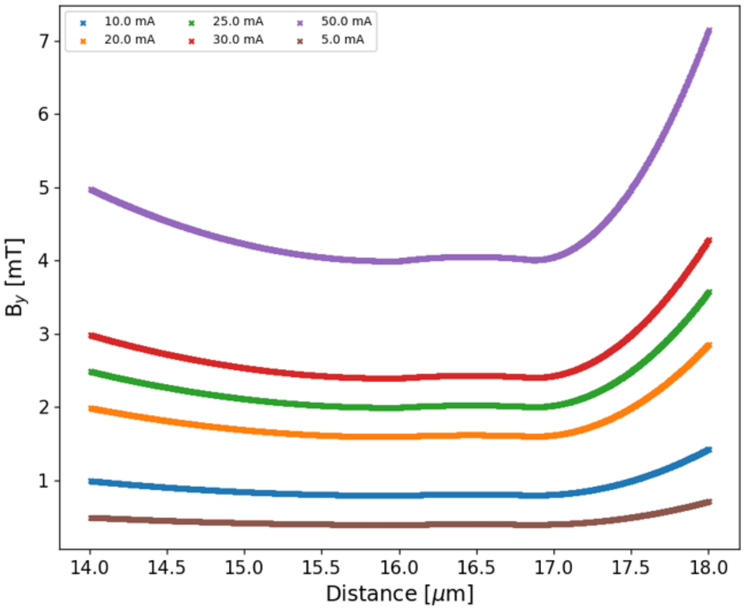

Figure 4.12: The trend of the y component of the magnetic field along the axis of the coils is illustrated on the x-axis, with the region in which the circular junction with a radius of $R = 2.5\mu m$ being the sole consideration.

The simulations were conducted with the understanding that the current proof-of-concept of the ferrotransmon is designed with the established fabrication of micrometric junctions. In light of the aforementioned dimensionality of the junctions, it can be posited that the line is more conducive to the ferrotrasmon architectural configuration. Furthermore, the fabrication of submicrometre junctions is progressing in accordance with the advancement of quantum technology, with the airbridge representing an optimal solution.

Finally, according to these simulations, we must further dilute the ferromagnetic alloy in order to switch it in the ranges of fields supported by the flux lines mentioned above. We have thus conducted a simulation of the Fraunhofer pattern (Figure 4.13) to estimate a plausible magnetization of the ferromagnetic layer M_F in order to observe a difference of the critical current at zero field of 30% after the application of a magnetic field pulse. A 30% variation of the critical current, as reported in reference 2.3, can lead to a tuning of the qubit frequency of 0.8 GHz. For the diameter and thickness of the SIsFS JJs investigated in this thesis, as shown in Figure 4.13 a magnetization of M_F of approximately 0.1 T is required.

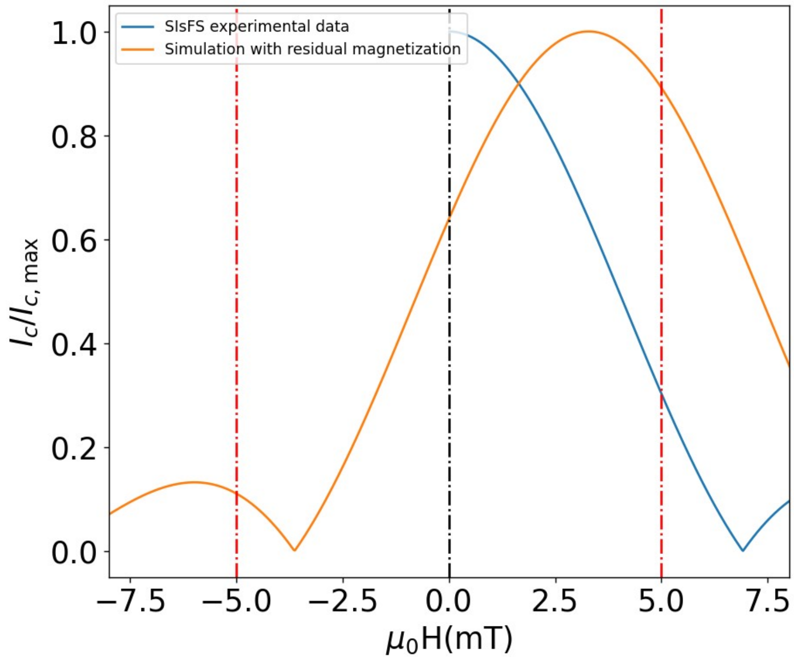

Figure 4.13: For SIsFS JJs with diameter of $4\mu m$ and thickness employed in this thesis a magnetization M_F of 0.1 T is required in order to provide a shift of the Fraunhofer pattern in order to achieve a 30% reduction of the critical current at zero field.

Conclusion

The ferrotransmon is an important proof of concept for superconducting quantum architectures, in which the use of tunnel magnetic Josephson Junctions allows an alternative tuning of the qubit frequency with important repercussions on the scalability of the entire circuit. For the development of the ferrotransmon, it is crucial to design a proper tunnel magnetic Josephson junction. We have thus started our investigation with a comparative analysis of the transport properties of SIsFS junctions employing a Permalloy ($Ni_{80}Fe_{20}$) layer as F barrier with a standard SIS tunnel junctions. We have observed that SIsFS junctions work effectively within the tunnel regime, exhibiting low dissipation and Josephson energy values compatible with the integration into this hybrid quantum circuit. The magnetic field response of SIsFS junctions exhibited hysteretic behavior, thus demonstrating that this layout can combine the memory properties of a magnetic JJ and the tunnel behaviour of a standard SIS JJ. However, in SIsFS junctions featuring a Permalloy layer a magnetic field of 50 mT is required to observe a significant shift in the junction pattern. Such a field strength presents a significant challenge in terms of practical implementation in quantum circuits, where the maintenance of low noise and high coherence times is of paramount importance. It is therefore evident that optimising the barrier represents a fundamental aspect of the ongoing development of the ferrotransmon architecture. In order to address this issue, we have conducted an investigation on the potential use of a diluted Permalloy barrier ($Ni_{70}Fe_{11}Gd_3Nb_9$). This approach demonstrated the ability to observe the required memory properties in a magnetic field range of -15 to 15 mT, representing a significant reduction of a factor 3 compared to the previous material. The successful demonstration of this dilution strategy highlights the potential for customising magnetic properties to achieve on-chip control of the junctions. By optimising the barrier, we can enhance the performance and reliability of the ferrotransmon architecture, enabling it to meet the stringent requirements of quantum computing applications. Looking forward, it is necessary to reduce the requisite magnetic fields and to design flux lines in a strategic way for this application. In contrast to standard flux-tunable transmons, which feature flux-bias lines inductively coupled to d.c. SQUID loops, standard SIsFS JJs require in-plane magnetic field to be switched. We have proposed three distinct designs, each of which aims at providing a 5 mT magnetic field on the ferromagnetic layer. In the case of micrometric Josephson junctions, the SCPW (superconducting coplanar waveguide) design is identified as the optimal solution, since it can provide more uniform magnetic fields. However, the SCPW, which is also more standard from the fabrication point of view, may introduce additional challenges due to its capacitive coupling with the qubit and may contribute to increased decoherence. The Helmholtz flux coil is expected to not significantly impact decoherence. The fact that these lines generate less uniform magnetic field can be mitigated by using submicrometric junctions, which are commonly employed in trasmon architectures. Therefore, it is crucial to acknowledge that junction optimization and flux line simulations complement each other in order to improve the ferrotransmon architecture for on-chip control. In order to achieve the ferrotransmon regime with a single SIsFS junction with a diameter of 4 μm, it is necessary that the ferromagnet switches in the range of (-5,5) mT and has a magnetization $M_F \sim$0.1 T. In conclusion, the integration of advanced materials and innovative designs shows great potential for improving qubit performance and deepening our understanding of the physics behind hybrid Josephson junctions. As we refine this architectural approach, we are poised to unlock new possibilities in quantum information processing, leading to a scalable quantum computing platform. Recognizing its strategic importance, the European Union has recently supported and expanded research in this area through the Ferromon project (Ferrotransmons and Ferrogatemons for Scalable Quantum Computers) [106].

Bibliography

[1] F. A. et al., “Quantum supremacy using a programmable superconducting processor,” Nature, vol. 574, pp. 505–510, oct 2019.

[2] S. Pirandola et al., ”Advances in quantum cryptography” Advances in Optics and Photonics Vol. 12, Issue 4, pp. 1012-1236 (2020), https://doi.org/10.1364/AOP.361502

[3] Martin, V., Brito, J.P., Escribano, C. et al. Quantum technologies in the telecommunications industry. EPJ Quantum Technol. 8, 19 (2021). https://doi.org/10.1140/epjqt/s40507-021-00108-9

[4] ”Superconducting Qubits: Current State of Play” Morten Kjaergaard et. al, Vol. 11:369-395 (Volume publication date March 2020) https://doi.org/10.1146/annurev-conmatphys-031119-050605.

[5] Jens Koch et al. “Charge-insensitive qubit design derived from the Cooper pair box”. In: Phys. Rev. A (2007). doi: 10.1103/PhysRevA.76.042319. url: https://link.aps.org/doi/10.1103/PhysRevA.76.042319.

[6] P. Krantz et al. “A quantum engineer’s guide to superconducting qubits”. In: Applied Physics Reviews (2019). doi: 10.1063/1.5089550.

[7] Halima Giovanna Ahmad et al. “Hybrid ferromagnetic transmon qubit: Circuit design, feasibility, and detection protocols for magnetic fluctuations”. In: Phys. Rev. B 105 (21 2022), p. 214522.

[8] M. Will et al., ”High Quality Factor Graphene-Based Two-Dimensional Heterostructure Mechanical Resonator”DOI: 10.1021/acs.nanolett.7b01845, Nano Lett. 2017, 17, 5950-5955

[9] Wang, J.IJ., Rodan-Legrain, D., Bretheau, L. et al. Coherent control of a hybrid superconducting circuit made with graphene-based van der Waals heterostructures. Nature Nanotech 14, 120–125 (2019). https://doi.org/10.1038/s41565-018-0329-2

[10] A. K. Feofanov, V. A. Oboznov, V. V. Bol’ginov, J. Lisenfeld, S. Poletto, V. V. Ryazanov, A. N. Rossolenko, M.

Khabipov, D. Balashov, A. B. Zorin, P. N. Dmitriev, V. P. Koshelets, and A. V. Ustinov, “Implementation of superconductor/ferromagnet/superconductor p-shifters in superconducting digital and quantum circuits,” Nat. Phys. 6, 593–597 (2010).

[11] Linder, J., Robinson, J. ”Superconducting spintronics.” Nature Phys 11, 307–315 (2015). https://doi.org/10.1038/nphys3242

[12] Birge, Norman O. (2018) Spin-triplet supercurrents in Josephson junctions containing strong ferromagnetic materials. Philosophical Transactions of the Royal Society A: Mathematical, Physical and Engineering Sciences, 376 (2125) 20150150 doi:10.1098/rsta.2015.0150

[13] L. Parlato, R. Caruso, A. Vettoliere, R. Satariano, H. G. Ahmad, A. Miano, D. Montemurro, D. Salvoni, G. Ausanio, F. Tafuri, G. P. Pepe, D. Massarotti, , and C. Granata, “Characterization of scalable Josephson memory element containing a strong ferromagnet,” J. Appl. Phys. 127, 193901, 2020.

[14] H. Ahmad, R. Satariano, R. Ferraiuolo, D. Massarotti ”Phase-dynamics of tunnel Al-based ferromagnetic Josephson junctions”, June 2024 124(232601) DOI: 10.1063/5.0211006

[15] Satariano, R., Volkov, A.F., Ahmad, H.G. et al. Nanoscale spin ordering and spin screening effects in tunnel ferromagnetic Josephson junctions. Commun Mater 5, 67 (2024). https://doi.org/10.1038/s43246-024-00497-1

[16] M. Tinkham. Introduction to Superconductivity: Second Edition. Dover Books on Physics. Dover Publications, 2004.

[17] Onnes, H.K. (1911) The Superconductivity of Mercury. Comm. Phys. Lab. Univ., Leiden, 122-124. Breyel, D., Schmidt, T.L. and Komnik, A. (2012) Rydberg Crystallization Detection by Statistical Means. Physical Review A, 86, Article ID: 023405. https://doi.org/10.1103/physreva.86.023405

[18] A. Barone and G. Paternò. Physics and applications of the Josephson effect. UMI Out-of-Print Books on Demand. Wiley, 1982.

[19] ”The Physics of Superconductors,Introduction to Fundamentals and Applications” V. V. Schmidt. Springer Berlin, Heidelberg. DOI https://doi.org/10.1007/978-3-662-03501-6

[20] Charles P. Poole, Horacio A. Farach, Richard J. Creswick, and Ruslan Prozorov. 12 - type II superconductivity. In Charles P. Poole, Horacio A. Farach, RichardJ.Creswick, andRuslanProzorov, editors, Superconductivity(Second Edition).AcademicPress,Amsterdam,secondeditionedition, 2007.

[21] "Possible new effects in superconductive tunnelling" Josephson, B. D. Physics Letters, Volume 1, Issue 7, p. 251-253. July 1962. DOI:10.1016/0031-63(62)91369-0

[22] Anderson, P. W.; Rowell, J. M. (15 March 1963). "Probable Observation of the Josephson Tunnel Effect". Physical Review Letters. 10 (6): 230. Bibcode:1963PhRvL..10..230A. doi:10.1103/PhysRevLett.10.230.

[23] Francesco Tafuri. Fundamentals and frontiers of the Josephson effect. Vol. 286. Springer Nature, 2019.

[24] B.D. Josephson, Supercurrents through barriers. Adv. Phys. 14, 419–451 (1965).

[25] K.K. Likharev, Dynamics of Josephson Junctions and Circuits (Gordon and Breach, NewYork, 1986).

[26] A. A. Golubov, M. Yu. Kupriyanov, and E. Il'ichev. "The current-phase relation in Josephson junctions". In: Rev. Mod. Phys. 76 (2 2004), pp. 411– 469. doi: 10.1103/RevModPhys.76.411.

[27] S. Shapiro. "Josephson Currents in Superconducting Tunneling: The Effect of Microwaves and Other Observations". In: Phys. Rev. Lett. 11 (2 1963), pp. 80–82. doi: 10.1103/PhysRevLett.11.80.

[28] P.W. Anderson, Special Effects in Superconductivity in Lectures on the Manybody Problem, in E.R. Caianiello, Ed. Ravello (1963) Vol. 2 (Academic, 1964), pp. 113–135

[29] Vinay Ambegaokar and Alexis Baratoff. "Tunneling Between Superconductors". In: Phys. Rev. Lett. 10 (11 June 1963), pp. 486–489. doi: 10 . 1103 / PhysRevLett.10.486. url: https://link.aps.org/doi/10.1103/PhysRevLett.10.486.

[30] John M. Martinis, Kevin Osborne. "Superconducting Qubits and the Physics of Josephson Junctions". Superconductivity (cond-mat.supr-con); Mesoscale and Nanoscale Physics (cond-mat.mes-hall). https://doi.org/10.48550/arXiv.cond-mat/0402415.

[31] W.C. Stewart, Current-voltage characteristics of Josephson junctions. Appl. Phys. Lett. 12, 277–280 (1968)

[32] D.E. McCumber, Effect of ac impedance on dc voltage-current characteristics of superconductor weak-link junctions. J. Appl. Phys. 39, 3113 (1968)

[33] D.G. McDonald, E.G. Johnson, R.E. Harris, Modeling Josephson junctions. Phys. Rev. B 13, 1028–1031 (1976)

[34] N.F. Pedersen, K. Saermark, Analytical solution for a Josephson-junction model with capacitance. Physica 69, 572–578 (1973).

[35] W.C. Scott, Hysteresis in the dc switching characteristics of Josephson junctions. Appl. Phys. Lett. 17, 166–168 (1970).

[36] Mi. H. Devoret, J. M. Martinis, and J. Clarke. “Measurements of Macroscopic Quantum Tunneling out of the Zero-Voltage State of a Current Biased Josephson Junction”. In: Phys. Rev. Lett. 55 (18 1985), pp. 1908–1911.

[37] J. M. Martinis, M. H. Devoret, and J. Clarke. “Experimental tests for the quantum behavior of a macroscopic degree of freedom: The phase difference across a Josephson junction”. In: Phys. Rev. B 35 (10 1987), pp. 4682–4698.

[38] J.M. Kivioja, T.E. Nieminen, J. Claudon, O. Buisson, F.W.J. Hekking, J.P. Pekola, ”Observation of transition from escape dynamics to underdamped phase diffusion in a Josephson junction.” Phys. Rev. Lett. 94, 247002 (2005)

[39] 67. J. Männik, S. Li, W. Qiu, W. Chen, V. Patel, S. Han, J.E. Lukens, Crossover from Kramers to phase-diffusion switching in moderately damped Josephson junctions. Phys. Rev. B 71, 220509 (2005)

[40] L. Longobardi, D. Massarotti, G. Rotoli, D. Stornaiuolo, G. Papari, A. Kawakami, G.P. Pepe, A. Barone, F. Tafuri, ”Thermal hopping and retrapping of a Brownian particle in the tilted periodic potential of a NbN/MgO/NbN Josephson junction.” Phys. Rev. B 84, 184504 (2011)

[41] ”Macroscopic quantum tunnelling in spin filter ferromagnetic Josephson junctions” D. Massarotti, A. Pal, G. Rotoli, L. Longobardi, M.G. Blamire, F. Tafuri. NATURE COMMUNICATIONS — 6:7376 — DOI: 10.1038/ncomms8376 — www.nature.com/naturecommunications.

[42] R.A. Voss, R.A. Webb, Macroscopic quantum tunneling in $1-\mu m$ Nb Josephson junctions. Phys. Rev. Lett. 47, 265 (1981)

[43] D. Massarotti et al.”A feasible path for the use of ferromagnetic josephson junctions in quantum circuits: The ferro-transmon” : Fiz. Nizk. Temp. 49, 871–880 (July 2023)

[44] A. F Kockum and F. Nori. “Quantum Bits with Josephson Junctions”. In: Fundamentals and Frontiers of the Josephson Effect. Ed. by F. Tafuri. Springer International Publishing, Cham, 2019, pp. 703–741.

[45] "The Physics of Nanoelectronics", First Edition, Tero T. Heikkilä, Tero T. Heikkilä 2013.Oxford University Press.

[46] "Introduction to quantum electromagnetic circuits" Uri Vool.

[47] Y. Nakamura, Y. A. Pashkin, and J. S. Tsai, “Coherent control of macroscopic quantum states in a single-Cooper-pair box,” Nature 398, 786 (1999).

[48] "An Introduction to the Transmon Qubit for Electromagnetic Engineers" Thomas E. Roth Member, IEEE, Ruichao Ma, and Weng C. Chew, IEE

[49] "Rabi Oscillations in a Large Josephson-Junction Qubit" John M. Martinis, S. Nam, J. Aumentado, and C. Urbina Phys. Rev. Lett. 89, 117901 – Published 21 August 2002

[50] "Qubit Architecture with High Coherence and Fast Tunable Coupling" Yu Chen et al., Phys. Rev. Lett. 113, 220502 – Published 26 November 2014

[51] M. D. Hutchings, J. B. Hertzberg, Y. Liu, N. T. Bronn, G. A. Keefe, M. Brink, J. M. Chow, and B. L. T. Plourde, “Tunable superconducting qubits with fluxindependent coherence,” Phys. Rev. Appl. 8, 044003 (2017).

[52] S. Chikazumi. Physics of Ferromagnetism. Oxford University Press, Oxford, 1997.

[53] Bernard Dennis Cullity and Chad D Graham. Introduction to magnetic materials. John Wiley & Sons, 2011.

[54] Stephen Blundell. Magnetism in condensed matter. OUP Oxford, 2001.

[55] E. C. Stoner. “Collective electron ferromagnetism”. In: Proc. R. Soc. Lond. A 165.922 (1938), pp. 372–414. doi: 10.1098/rspa.1938.0066.

[56] "Influence of boundary transparency on the critical current of "dirty" SS'S structures" M. Yu. Kupriyanov and V. F. Lukichev, Zh. Eksp. Teor. Fiz. 94,139-149 (June 1988).

[57] A. I. Buzdin "Proximity effects in superconductor-ferromagnet heterostructures."REVIEWS OF MODERN PHYSICS, VOLUME 77, JULY 2005

[58] "Proximity effect in normal metal–multiband superconductor hybrid structures" A. Brinkman, A. A. Golubov, and M. Yu. Kupriyanov, Phys. Rev. B 69, 214407 – Published 4 June 2004.

[59] I.O. Kulik, A.N. Omelyanchuk, Contribution to the microscopic theory of the Josephson effect in superconducting bridges. Pis'ma v Zh. Eksp. Teor. Fiz. 21, 216–217 (1975). JETP Lett. 21, 96–97 (1975)

[60] I.O. Kulik, A.N. Omelyanchuk, Properties of superconducting microbridges in the pure limit. Fiz. Nizk.-Temp. 4, 945–946 (1977); Sov. J. Low Temp. Phys. 3, 459–460 (1977)

[61] K.K. Likharev, Superconducting weak links. Rev. Mod. Phys. 51, 101–159 (1979)

[62] O. M. Kapran et al. "Crossover between short- and long-range proximity effects in superconductor/ferromagnet/superconductor junctions with Ni-based ferromagnets". In: Phys. Rev. B 103 (9 2021), p. 094509. doi: 10. 1103/PhysRevB.103.094509.

[63] "Low−energy excitations and magnetic anisotropy of the layered van der Waals antiferromagnet $Ni_2P_2S_6$". K. Mehlawat, A. Alfonsov, S. Selter, Y. Shemerliuk, S. Aswartham, B. B$\ddot{u}$chner, and V. Kataev Phys. Rev. B 105, 214427, Published 22 June 2022.

[64] "Coupling of Two Superconductors through a Ferromagnet: Evidence for a π Junction" V. V. Ryazanov, V. A. Oboznov, A. Yu. Rusanov, A. V. Veretennikov, A. A. Golubov, and J. Aarts Phys. Rev. Lett. 86, 2427 – Published 12 March 2001

[65] "Thickness Dependence of the Josephson Ground States of Superconductor-Ferromagnet-Superconductor Junctions" V. A. Oboznov, V. V. Bol'ginov, A. K. Feofanov, V. V. Ryazanov, and A. I. Buzdin. Phys. Rev. Lett. 96, 197003 – Published 19 May 2006

[66] Norman O. Birge, Nathan Satchell "Ferromagnetic Materials for Josephson π Junctions" https://doi.org/10.48550/arXiv.2401.04219, APL Materials 12, 041105 (2024)

[67] H. Sellier et al. "Half-Integer Shapiro Steps at the $0-\pi$ Crossover of a Ferromagnetic Josephson Junction". In: Phys. Rev. Lett. 92 (25 2004), p. 257005.

[68] Pal, A., Barber, Z., Robinson, J. et al. Pure second harmonic current-phase relation in spin-filter Josephson junctions. Nat Commun 5, 3340 (2014). https://doi.org/10.1038/ncomms4340

[69] N. Banerjee et al. "Evidence for spin selectivity of triplet pairs in superconducting spin valves". In: Nat. Commun. 5 (2014), p. 3048.

[70] N. Banerjee, J. W. A. Robinson, and M. G. Blamire. “Reversible control of spin-polarized supercurrents in ferromagnetic Josephson junctions”. In: Nat. Commun. 5 (2014), p. 4771.

[71] F. S. Bergeret et. al. ”Odd triplet superconductivity and related phenomena in superconductor-ferromagnet structures” DOI:https://doi.org/10.1103/RevModPhys.77.1321, 2005 American Physical Society.

[72] V. V. Bol’ginov et al. “Magnetic switches based on Nb-PdFe-Nb Josephson junctions with a magnetically soft ferromagnetic interlayer”. In: JETP Lett. 95 (2012), p. 366.

[73] T. S. Khaire, W. P. Pratt, and N. O. Birge. “Critical current behavior in Josephson junctions with the weak ferromagnet PdNi”. In: Phys. Rev. B 79 (2009), p. 094523.

[74] ”Ferromagnetic Josephson switching device with high characteristic voltage” Timofei I. et. al Appl. Phys. Lett. 100, 222601 (2012); doi: 10.1063/1.4723576

[75] S. V. Bakurskiy et al. “Theory of supercurrent transport in SIsFS Josephson junctions”. In: Phys. Rev. B 88 (14 2013), p. 144519. doi: 10.1103/ PhysRevB.88.144519. url: https://link.aps.org/doi/10.1103/ PhysRevB.88.144519.

[76] M. Weides. “Magnetic anisotropy in ferromagnetic Josephson junctions”. In: Applied Physics Letters 93.5 (Aug. 2008). doi: 10.1063/1.2967873. url: https://doi.org/10.1063% 2F1.2967873.

[77] A. S. Vasenko, A. A. Golubov, M. Yu. Kupriyanov, and M. Weides. “Properties of tunnel Josephson junctions with a ferromagnetic interlayer”. In: Phys. Rev. B 77 (13 Apr. 2008), p. 134507. doi: 10.1103/PhysRevB.77.134507. url: https://link.aps.org/doi/10.1103/PhysRevB.77.134507.

[78] S. V. Bakurskiy et al. “Theoretical model of superconducting spintronic SIsFS devices”. In: Appl. Phys. Lett. 102.19 (2013), p. 192603. doi: 10.

[79] Himmel, Nico. ”Josephson junctions with ferromagnetic alloy interlayer.” (2015). 1063/1.4805032.

[80] Ryazanov, V et. al. (2012). ”Magnetic Josephson Junction Technology for Digital and Memory Applications.” Physics Procedia. 36. 35-41. 10.1016/j.phpro.2012.06.126.

[81] T. I. Larkin et al. “Ferromagnetic Josephson switching device with high characteristic voltage”. In: Appl. Phys. Lett. 100 (2012), p. 222601.

[82] I. V. Vernik et al. “Magnetic Josephson Junctions With Superconducting Interlayer for Cryogenic Memory”. In: IEEE Trans. Appl. Supercond. 23.3 (2013), pp. 1701208–1701208. doi: 10.1109/TASC.2012.2233270.

[83] MRS Bulletin , Volume 38 , Issue 10: Materials issues for quantum computation, October 2013 , pp. 816 - 825. DOI: https://doi.org/10.1557/mrs.2013.229

[84] R. Aguado ”A perspective on semiconductor-based superconducting qubits” Appl. Phys. Lett. 117, 240501 (2020); https://doi.org/10.1063/5.0024124.

[85] ”Semiconductor-Nanowire-Based Superconducting Qubit”T.W. Larsen, K.D. Petersson, F. Kuemmeth, T.S. Jespersen, P. Krogstrup, J. Nygård, and C.M. Marcus. Phys. Rev. Lett. 115, 127001 – Published 14 September 2015

[86] S. Kim, L.V. Abdurakhimov, D. Pham, W. Qiu, H. Terai, S. Ashhab, S. Saito, T. Yamashita, K.Semba: ”Superconducting flux qubit with ferromagnetic Josephson π junction operating at zero magnetic field”.

[87] ”Impact of a ferromagnetic insulating barrier in magnetic tunnel junctions.” M. Abbasi Eskandari, S. Ghotb, P. Fournier. https://doi.org/10.48550/arXiv.2212.04416

[88] C. Rigetti, J. M. Gambetta, S. Poletto, B. L. T. Plourde, J. M. Chow, A. D. Córcoles, J. A. Smolin, S. T. Merkel, J. R. Rozen, G. A. Keefe, M. B. Rothwell, M. B. Ketchen, and M. Steffen, ”Superconducting qubit in a waveguide cavity with a coherence time approaching 0.1 ms”, Phys. Rev. B 86, 100506(R) (2012).

[89] A. Blais, R.-S. Huang, A. Wallraff, S. M. Girvin, and R. J. Schoelkopf, ”Cavity quantum electrodynamics for superconducting electrical circuits: An architecture for quantum computation”, Phys. Rev. A 69, 062320 (2004).

[90] L. N. Karelina, R. A. Hovhannisyan, I. A. Golovchanskiy, et al.”Scalable memory elements based on rectangular SIsFS junctions” J. Appl. Phys. 130, 173901 (2021); https://doi.org/10.1063/5.0063274. 01 November 2021.

[91] ”Historical Summary of Cryogenic Activity Prior to 1950”R. Radebaugh, January 2007. DOI: 10.1007/0-387-46896-X_1.

[92] R. Caruso *et al.*, ”Properties of Ferromagnetic Josephson Junctions for Memory Applications,” in *IEEE Transactions on Applied Superconductivity*, vol. 28, no. 7, pp. 1-6, Oct. 2018, Art no. 1800606, doi: 10.1109/TASC.2018.2836979.

[93] Bol'ginov, V.V., Tikhomirov, O.A. and Uspenskaya, L.S. Two-component magnetization in Pd99Fe01 thin films. *Jetp Lett.* **105**, 169–173 (2017). https://doi.org/10.1134/S0021364017030055

[94] J. C. Lee, W. D. Oliver, K. K. Berggren, and T. P. Orlando, "Nonlinear resonant behavior of a dispersive readout circuit for a superconducting flux qubit", Phys. Rev. B, Volume 75, 2007, 144505,10.1103/PhysRevB.75.144505

[95] J. Lisenfeld, A. Lukashenko, M. Ansmann, J. M. Martinis, and A. V.Ustinov, "Temperature Dependence of Coherent Oscillations in Josephson Phase Qubits", Phys. Rev. Lett., Volume 99, 2007, 170504, 10.1103/PhysRevLett.99.170504

[96] E. Hoskinson, F. Lecocq, N. Didier, A. Fay, F. W. J. Hekking, W. Guichard, O. Buisson, R. Dolata, B. Mackrodt, and A. B. Zorin, Quantum Dynamics in a Camelback Potential of a dc SQUID", Phys. Rev. Lett., Volume 102, 2009, 097004, 10.1103/PhysRevLett.102.097004

[97] Vettoliere, Antonio, Roberta Satariano, Raffaella Ferraiuolo, Luigi Di Palma, Halima Giovanna Ahmad, Giovanni Ausanio, Giovanni Piero Pepe, Francesco Tafuri, Davide Massarotti, Domenico Montemurro, and et al. 2022. "High-Quality Ferromagnetic Josephson Junctions Based on Aluminum Electrodes" Nanomaterials 12, no. 23: 4155. https://doi.org/10.3390/nano12234155

[98] . A. Vettoliere, R. Satariano, R. Ferraiuolo, L. Di Palma, H. G. Ahmad, G. Ausanio, G. P. Pepe, F. Tafuri, D. Montemurro, C. Granata, L. Parlato, D. Massarotti; Aluminum-ferromagnetic Josephson tunnel junctions for high quality magnetic switching devices. *Appl. Phys. Lett.* 27 June 2022; 120 (26): 262601.

[99] P. Silvestrini, R. Russo, V. Corato, B. Ruggiero, C. Granata, S. Rombetto, M. Russo, M. Cirillo, A. Trombettoni, P. Sodano, Topology-induced critical current enhancement in Josephson networks, Physics Letters A, 2007, 370, 499-503, https://doi.org/10.1016/j.physleta.2007.05.119.

[100] "Merged-Element Transmons: Design and Qubit Performance." H. J. Mamin et al. Phys. Rev. Applied 16, 024023 (2021) https://doi.org/10.1103/PhysRevApplied.16.024023

[101] H. Szymczak,"Magnetic Materials and Applications", Encyclopedia of Condensed Matter Physics,2005, Pages 204-211, https://doi.org/10.1016/B0-12-369401-9/00523-4.

[102] Birge, Norman O. (2018) Spin-triplet supercurrents in Josephson junctions containing strong ferromagnetic materials. Philosophical Transactions of the Royal Society A: Mathematical, Physical and Engineering Sciences, 376 (2125) 20150150 doi:10.1098/rsta.2015.0150

[103] "Inverse magnetic hysteresis of the Josephson supercurrent: Study of the magnetic properties of thin niobium/permalloy ($Fe_{20}Ni_{80}$) interfaces".Satariano, R. et al. Phys. Rev. B 10322224521,2021Jun,American Physical Society,doi10.1103/PhysRevB.103.224521

[104] Xuehua Zhu, Meng Xing, Chuangchuang Liu, Juntao Ye, Hongde Cheng, Yutong Miao, "Optimization of composite Helmholtz coils towards high magnetic uniformity" Engineering Science and Technology, an International Journal, Volume 47, 2023, https://doi.org/10.1016/j.jestch.2023.101539.

[105] Rahime Alsangur, Serkan Doğanay, Ismet Ates, Alpaslan Turgut, Levent Cetin, "3D Helmholtz coil system setup for thermal conductivity measurements of magnetic nanofluids" Mechatronics,Volume 94,2023,103019, https://doi.org/10.1016/j.mechatronics.2023.103019.

[106] https://ferromon.eu/ferromon-project